Fermi National Accelerator Laboratory

FERMILAB-Pub-93/246

E665

Production of Charged Hadrons by Positive Muons on Deuterium and Xenon at 490 GeV

M.R. Adams et al
The E665 Collaboration

Fermi National Accelerator Laboratory
P.O. Box 500, Batavia, Illinois 60510

August 1993

Submitted to *Zeitschrift fur Physik C*

Operated by Universities Research Association Inc. under Contract No. DE-AC02-76CHO3000 with the United States Department of Energy

Disclaimer

Production of charged hadrons by positive muons on deuterium and xenon at 490 GeV

THE E665 COLLABORATION

August 1993

Submitted to Zeitschrift für Physik C

Abstract

Results on the production of charged hadrons in muon-deuteron and muon-xenon interactions are presented. The data were taken with the E665 spectrometer, which was exposed to the 490 GeV muon beam of the Tevatron at Fermilab. The use of a streamer chamber as vertex detector provides nearly 4π acceptance for charged particles. The μD data are compared with the μXe data in terms of multiplicity distributions, average multiplicities, forward-backward multiplicity correlations, rapidity and transverse momentum distributions and of two-particle rapidity correlations of charged hadrons. The data cover a range of invariant hadronic masses W from 8 to 30 GeV.

M. R. Adams [6], M. Aderholz [11], S. Aïd [9,a], P. L. Anthony [10,b], M. D. Baker [10], J. Bartlett [4], A. A. Bhatti [13,c], H. M. Braun [14], W. Busza [10], J. M. Conrad [5], G. Coutrakon [4,d], R. Davisson [13], I. Derado [11], S. K. Dhawan [15], W. Dougherty [13], T. Dreyer [1], K. Dziunikowska [8], V. Eckardt [11], U. Ecker [14,a], M. Erdmann [1,e], A. Eskreys [7], J. Figiel [7], H. J. Gebauer [11], D. F. Geesaman [2], R. Gilman [2,f], M. C. Green [2,g], J. Haas [1], C. Halliwell [6], J. Hanlon [4], D. Hantke [11], V. W. Hughes [15], H. E. Jackson [2], D. E. Jaffe [6,h], G. Jancso [11], D. M. Jansen [13,i], S. Kaufman [2], R. D. Kennedy [3], T. Kirk [4,j], H. G. E. Kobrak [3], S. Krzywdzinski [4], S. Kunori [9], J. J. Lord [13], H. J. Lubatti [13], D. McLeod [6], S. Magill [6,j], P. Malecki [7], A. Manz [11], H. Melanson [4], D. G. Michael [5,k], W. Mohr [1], H. E. Montgomery [4], J. G. Morfin [4], R. B. Nickerson [5,l], S. O'Day [9,m], K. Olkiewicz [7], L. Osborne [10], V. Papavassiliou [15,j], B. Pawlik [7], F. M. Pipkin [5,n], E. J. Ramberg [9,m], A. Röser [14,o], J. J. Ryan [10], C. W. Salgado [4], A. Salvarani [3,p], H. Schellman [12], M. Schmitt [5,q], N. Schmitz [11], K. P. Schüler [15,r], H. J. Seyerlein [11], A. Skuja [9], G. A. Snow [9], S. Söldner-Rembold [11,s], P. H. Steinberg [9], H. E. Stier [1], P. Stopa [7], R. A. Swanson [3], R. Talaga [9,j], S. Tentindo-Repond [2,t], H.-J. Trost [2,u], H. Venkataramania [15], M. Wilhelm [1], J. Wilkes [13], Richard Wilson [5], W. Wittek [11], S. A. Wolbers [4], T. Zhao [13]

(E665 Collaboration)

[1] *Albert-Ludwigs-Universität Freiburg i. Br., Germany*
[2] *Argonne National Laboratory, Argonne IL USA*
[3] *University of California, San Diego, CA USA*
[4] *Fermi National Accelerator Laboratory, Batavia, IL USA*
[5] *Harvard University, Cambridge, MA USA*
[6] *University of Illinois, Chicago, IL USA*
[7] *Institute for Nuclear Physics, Krakow, Poland*
[8] *Institute for Nuclear Physics, Academy of Mining and Metallurgy, Krakow, Poland*
[9] *University of Maryland, College Park, MD USA*
[10] *Massachusetts Institute of Technology, Cambridge, MA USA*
[11] *Max-Planck-Institut für Physik, Munich, Germany*
[12] *Northwestern University, Evanston, IL USA*
[13] *University of Washington, Seattle, WA USA*
[14] *University of Wuppertal, Wuppertal, Germany*
[15] *Yale University, New Haven, CT USA*

[a] Current address: Alaskaweg 20, 22145 Hamburg 73, Germany.
[b] Current address: Lawrence Livermore National Laboratory, Livermore CA 94550, USA.
[c] Current address: The Rockefeller University, New York NY 10021, USA.
[d] Current address: Loma Linda University Medical Center, Loma Linda CA 92350, USA.
[e] Current address: DESY, Notkestrasse 85, 22603 Hamburg, Germany.
[f] Current address: Rutgers University, Piscataway, NJ 08855, USA.
[g] Current address: LeCroy Research Systems, Spring Valley, NY 10977, USA.
[h] Current address: Laboratoire de l'Accèlèrateur Linèaire, F-91405 Orsay, France.
[i] Current address: Los Alamos National Laboratory, Los Alamos, NM 87545, USA.
[j] Current address: Argonne National Laboratory, Argonne, IL 60439, USA.
[k] Current address: California Institute of Technology, Pasadena, CA 91125, USA.
[l] Current address: Oxford University, Oxford OX1 3RH, UK.
[m] Current address: Fermi National Accelerator Laboratory, Batavia, IL 60510, USA.
[n] Deceased
[o] Current address: Universität Bochum, 44801 Bochum, Germany.
[p] Current address: A.T. & T., Bell Labs, 2000 North Naperville Road, Naperville, IL USA.
[q] Current address: University of Wisconsin, Madison, WI 53706, USA.
[r] Current address: Superconducting Super Collider Laboratory, Dallas, TX 75237, USA.
[s] Current address: Albert-Ludwigs-Universität Freiburg, 79104 Freiburg, Germany.
[t] Current address: Northern Illinois University, Dekalb, IL 60115, USA.
[u] Current address: Texas A&M University, College Station, Texas 77843-4242

1 Introduction

Hadron production in deep-inelastic muon-nucleon scattering has been studied in several experiments, using light [1, 2, 3] and heavy targets [4, 5, 6]. The general features of the data can be understood in the framework of the quark-parton model (QPM), in which the virtual photon, emitted by the incoming muon, interacts with a parton of the target nucleon. In Fig. 1 this process is sketched as seen in the center-of-mass system of the virtual-photon and nucleon: the struck parton is emitted into the forward direction, while the target remnant travels into the backward direction. Both the struck parton and the target remnant fragment (hadronize) into observable hadrons, forming forward and backward jets.

According to this picture, data on hadron production give information on the distribution of the partons in the nucleon (or nucleus) and on the hadronization process. This particular analysis deals with hadron production in deep-inelastic muon-deuteron and muon-xenon scattering. The experiment uses a streamer chamber as vertex detector, providing nearly 4π acceptance for charged hadrons. Thus a measurement of both the forward and the backward hemisphere in the hadronic center-of-mass system is possible. The experiment extends previous measurements of the hadronic system in muon-nucleon scattering into a region of higher invariant hadronic mass W, up to values of $W \approx 30$ GeV. Measurements are presented on multiplicity distributions, on average multiplicities, on forward-backward multiplicity correlations, on rapidity and transverse momentum distributions and on two-particle rapidity correlations of charged hadrons.

The use of two targets, a liquid D and a gaseous Xe target, allows the study of hadron production on quasifree nucleons as well as on a heavy nucleus. It is the first experiment in which the complete hadronic final state (with respect to charged hadrons) is measured in deep-inelastic muon scattering on a heavy nucleus. The Xe data are compared with D data to obtain information on the formation and the cascading of hadrons in nuclear matter.

Measuring the cascade process is of great importance for the understanding of the space-time development of particle production processes [7]. However, due to multiple projectile collisions in the nucleus, it is rather difficult to identify the cascade processes in hadron-nucleus collisions. On the other hand there is a possibility of identifying cascade processes in lepton-induced reactions, where multiple collisions of the projectile (which in this case is the virtual photon) are expected to be strongly suppressed [8, 9, 10, 11].

The deep-inelastic muon-nucleon scattering process can be described by the exchange of a single virtual photon. In the following the target nucleon is assumed to be at rest in the laboratory frame, which means that the internal momenta of the nucleons within the nucleus are ignored. The kinematic variables of the event are then defined by

$$Q^2 = -2m_\mu^2 + 2E_\mu E'_\mu - 2p_\mu p'_\mu \cos\Theta \qquad \text{negative square of the virtual photon four-momentum,}$$

$$W^2 = -Q^2 + 2M\nu + M^2 \qquad \text{squared invariant mass of the hadronic system,}$$

$$x_{Bj} = \frac{Q^2}{2M\nu} \qquad \text{Bjorken-x,} \tag{1}$$

$$\nu = E_\mu - E'_\mu \qquad \text{leptonic energy transfer in the laboratory frame,}$$

where m_μ is the muon mass, E_μ (E'_μ) is the laboratory energy and p_μ (p'_μ) the laboratory momentum of the incident (outgoing) muon, Θ is the muon scattering angle in the laboratory frame and M is the nucleon mass.

The hadron variables used are Feynman-x, $x_F = 2p^*_L/W$, the laboratory and cms rapidities

$$y_{lab} = \frac{1}{2}\ln\frac{E_h + p_L}{E_h - p_L}\,, \quad y^* = \frac{1}{2}\ln\frac{E^*_h + p^*_L}{E^*_h - p^*_L}$$

and the transverse momentum p_T. E_h, p_L and p_T are the energy, the longitudinal and transverse momentum (relative to the direction of the virtual photon) of the hadron in the laboratory frame. The hadronic center-of-mass frame (cms) is defined by the system formed by the virtual photon and the target nucleon, and the variables in this frame are labelled by a $*$. The forward and backward hemispheres correspond to the regions x_F (or y^*) > 0 and x_F (or y^*) < 0, respectively.

The layout of the paper is as follows: Sect. 2 describes the experimental setup and the trigger used. The experimental procedure is explained in Sect. 3, while Sect. 4 deals with the simulation of the experiment and the correction of the experimental data. Some theoretical terms are explained in Sect. 5 and the experimental results are presented in Sect. 6. A summary is given in Sect. 7.

2 The experiment

The data were taken in the years 1987–1988 using the E665 spectrometer in the muon beamline of the Fermilab Tevatron. The muon beam had an average energy of 490 GeV with a dispersion of approximately 60 GeV. The muon beam impinged on a target filled either with liquid hydrogen (H), deuterium (D) or gaseous Xenon (Xe). Only the D and Xe data sets are used in the present analysis. The main parameters of the targets are listed in Table 1.

A streamer chamber (SC), surrounding the target and located inside a 4.3 Tm vertex magnet (CVM), provides momentum measurement of nearly all low momentum charged hadrons ($0.2 < p < 10$ GeV/c). The scattered muon and high momentum ($p \gtrsim 10$ GeV/c) charged hadrons are reconstructed and measured by a forward spectrometer (FS) which comprises a second magnet (CCM with - 6.7 Tm) and several sets of proportional and drift chambers. Photons are detected with an electromagnetic calorimeter. Downstream of an iron absorber for the hadrons, the scattered muon

is detected and reconstructed by several sets of proportional tubes and scintillation counters.

The requirements of the trigger (LAT.PCN trigger) used in the present analysis can be described as follows: a well defined beam track, no signal in the halo veto counters, signals in 3 (out of 4) muon scintillator planes (implying a cut in the muon scattering angle of approximately $\Theta \geq 3$ mr) and no signals close to the beam axis in the veto counters of the muon detector. In addition, in order to enhance the fraction of deep-inelastic events in the SC pictures, at least two hits are required in the non-bending planes of the PCN detector (outside the beam region), which is a proportional chamber located in the field free region between the two magnets. A detailed description of the apparatus and of the triggers has been published elsewhere [12].

In the present analysis only those events are included for which a streamer chamber picture was taken. The analysis is described in detail in reference [13].

3 Experimental procedure

3.1 Measurement of muons, hadrons and of electromagnetic energy

Muons are identified by matching the track segments downstream of the hadron absorber with the particle trajectories reconstructed using the detectors upstream of the absorber. In case of multiple combinations between track segments upstream and downstream of the absorber, the combinations with the highest χ^2-probabilities are accepted. Monte Carlo studies show that the rate of misidentification is very low.

Only hadrons fitted to the primary vertex, defined by the incident and outgoing muon, are counted as primary tracks. The mean position error (transverse to the track direction) of a track at the primary vertex is about 1.7 mm for tracks measured with the forward spectrometer (FS tracks) and about 1.4 cm for those measured with the streamer chamber (SC tracks). The mean momentum error $\Delta p/p$ is $5 \times 10^{-5} p/(\mathrm{GeV}/c)$ for FS and $0.02\ p/(\mathrm{GeV}/c)$ for SC tracks.

Hadrons emitted at small scattering angles are detected by both the SC and by the FS. A special selection procedure is applied to avoid double counting of these particles. Whenever available, the track parameters as determined by the reconstruction in the FS are used in the analysis. As a consequence, the 3-momentum of most particles with $y^* < 1$ is determined by the SC and of most particles with $y^* > 1$ by the FS.

The information from the particle identification detectors in the E665 spectrometer was not available for this analysis. Instead a partial identification of protons is performed, based on physics expectations. A Monte-Carlo calculation (using the Lund model) shows that in μD scattering, with $E_\mu = 490$ GeV and $W > 8$ GeV, the majority of the positive hadrons with $x_F(m_\pi) < -0.2$ are protons ($x_F(m_\pi)$ is x_F of a particle calculated as if it were a pion). Therefore all positive hadrons in the data with $x_F(m_\pi)$ less than -0.2 are assigned the proton mass, all other hadrons are treated as pions. The systematic error due to this procedure (and to the use of an incomplete Monte

Carlo) in the rapidity distribution of positive hadrons in the μXe reaction is discussed in Sect. 6.2.

The mimimum laboratory momentum p required for any hadron is 200 MeV/c, because protons with lower momenta are often absorbed in the target or in the target wall. In the data analysis no correction is applied for this cut. This means that all results presented in Sect. 6, in particular the average multiplicities, normalized rapidity and transverse momentum distributions, refer to hadrons with $p > 200$ MeV/c.

Electromagnetic energy is measured by the calorimeter with a resolution of

$$\frac{\sigma}{E} = 0.07 + \frac{0.45}{\sqrt{E/\mathrm{GeV}}}.$$

In the analysis, the information of the calorimeter is used to identify events which are due to muon bremsstrahlung (see Sect. 3.3).

3.2 Systematic errors

The systematic errors for the Xe and D data sets have different origins and in addition do not necessarily cancel in Xe/D ratios; therefore they are studied separately.

Hadrons, produced in a primary muon interaction, may undergo secondary interactions in the target and produce more particles. The vertex finding program is only partly able to identify those hadrons which originate from a secondary interaction. Thus some of them are erroneously associated to the primary vertex, leading to a contamination of primarily produced particles. Although this contamination, which depends on the vertex position along the target axis, is corrected by Monte Carlo (MC) calculations, there remains a weak dependence of the corrected multiplicity on the vertex position, from which a systematic error $\Delta\bar{n}$ of the average multiplicity is determined. For the D target $\Delta\bar{n}$ is estimated to be ± 0.35. Because of the much smaller number of interaction lengths (Table 1), secondary interactions in the Xe target and their effect on $\bar{n}$ can be neglected.

Due to slightly different interpretations of the scanning and measuring rules and to the different resolution of measuring devices at the two laboratories (MPI and FNAL) which measured the streamer chamber pictures, small differences between the corrected multiplicities from the two laboratories are observed. They suggest an additional systematic error $\Delta\bar{n}$ of 0.20 for the D and 0.25 for the Xe target.

For the D target a systematic error of $\Delta\bar{n} = 0.1$ due to uncertainties of the MC model (used for the correction of the experimental data, see Sect. 4) is determined.

An important source of systematic error on the average multiplicity in the Xe data is the use of an incomplete MC model: nuclear effects in the target nucleus, e.g. reinteractions of hadrons in the Xe nucleus, are not included, resulting in systematically lower multiplicities in the MC simulation than in the data. This leads to an uncertainty of the corrections (see Sect. 4), implying a systematic error of $\Delta\bar{n} = 0.3$ in the Xe data.

For both targets the systematic error $\Delta\bar{n}$ due to uncertainties in the simulation of the trigger, in particular the requirement on PCN hits, is estimated to be 0.10.

The overall systematic error of the average total multiplicity of charged hadrons is 0.43 (0.40) for the D (Xe) target, after adding the individual contributions in quadrature (Table 2).

In a similar manner a systematic error $\Delta(1/k)$ of the parameter $1/k$ in a negative binomial parametrization (see eq.(6)) of the multiplicity distribution is estimated and found to be $\Delta(1/k) = 0.01$ for the D and 0.03 for the Xe target.

In the Xe target, photons (mainly from π^0 decays) convert into electron-positron pairs with high probability. Some of these electrons and positrons are attached to the primary muon interaction and mistaken for charged hadrons. In the MC events about 16% of the tracks fitted to the primary vertex are actually electrons. In principle the contamination of hadrons by electrons should be taken care of by the correction procedure, however, in certain regions of phase space the corrections are very large, leading to an additional uncertainty. The corrections are especially large for $p_T^2 \lesssim 0.02$ $(\mathrm{GeV/c})^2$ and are different for μXe and μD scattering. In the μXe/μD ratio of the p_T distributions (Fig. 27) the larger contamination from secondary interactions in μD is partly compensated by the larger contamination from electrons in μXe scattering. Although the correction factors for the ratio in this p_T^2 region deviate from 1 by less than 0.2, the ratio has a large systematic error ($\approx 20\%$) due to the large correction factors for the individual p_T^2 distributions for μD and μXe scattering.

If not stated explicitly otherwise all errors drawn in the figures and quoted in the text and in the tables are statistical only.

3.3 Selection of the data

The initial event sample consists of those events for which a primary vertex was reconstructed within the target, using the beam track and the tracks reconstructed in the FS, and which fulfill the requirements of the LAT.PCN trigger (see Sect. 2). An event has to be identified in the SC, which means that the presence of at least one SC track, clearly distinguishable from the throughgoing beam tracks, is required. In addition, a set of kinematic cuts is applied to define the deep-inelastic region (high Q^2 and W), to avoid kinematic regions where radiative corrections are large (high ν/E_μ, low x_{Bj}) and to exclude the region where the experimental resolution is poor (low ν/E_μ):

$$\begin{aligned} \Theta &> 3.5 \text{ mr} \\ Q^2 &> 1 \text{ GeV}^2 \\ 8 &< W < 30 \text{ GeV} \\ x_{Bj} &> 0.002 \\ 0.1 &< \nu/E_\mu < 0.85 \end{aligned} \tag{2}$$

After these cuts, events with QED bremsstrahlung from muons interacting coherently with the Xe nucleus still constitute a sizeable fraction of the μXe events at high ν/E_μ. In addition, both data sets still contain deep-inelastic events with a high-energy bremsstrahlung photon in the final state. In order to eliminate these bremsstrahlung

events an additional cut on the energy deposited in the calorimeter is applied for both the Xe and D data set:

an event is removed

- if the number of energy clusters in the calorimeter is ≤ 2 or, alternatively, if the highest-energy cluster contains more than 80% of the total energy deposited in the calorimeter
- and if, in addition, the total energy deposited in the calorimeter is $\geq 0.5\ \nu$.

This cut eliminates about 8% of the μXe and 6% of the μD events.

For compatibility with another analysis of data from this experiment [14], a further cut is applied which mainly removes events due to diffractive ρ^0 production or which contain a bremsstrahlung photon and no additional charged hadron: an event is rejected if in addition to the scattered muon there is only one pair of oppositely charged particles in the final state, and if the effective mass of this pair is compatible with a photon conversion (electron-positron effective mass less than 0.20 GeV) or with a ρ^0 decay (effective $\pi^+\pi^-$ mass between 0.57 and 0.97 GeV). This cut removes less than 0.5% of the events.

After all cuts, the total number of events is 6309 for the D and 2064 for the Xe target. The number of events in different W bins is listed in Table 3, together with the respective average values of W, x_{Bj} and ν. The raw distributions of W, Q^2, ν and x_{Bj} for the final samples of μD and μXe events are displayed in Fig. 2.

4 Simulation of the experiment and correction of the experimental data

The Monte Carlo simulation of an event includes the following steps:

- generation of the event (including radiative effects),
- simulation of the detector response, taking into account chamber inefficiencies, secondary interactions, particle decays and photon conversions,
- simulation of the trigger,
- reconstruction of the event, using the same chain of programs as for the reconstruction of real events.

The events are generated using the LEPTO 4.3/JETSET 4.3 [15] version of the LUND program. The radiative effects are calculated with the program GAMRAD [16], which is based on the work in ref. [17]. The complete detector is simulated by a GEANT [18] based Monte Carlo program.

The acceptance and the response of the calorimeter were not simulated in the Monte Carlo program. The effect of the cut on muon bremsstrahlung events (see Sect. 3.3) was therefore simulated by a simplified model.

The ratio of the number of reconstructed to the number of generated events (in the kinematic region defined by eq. (2)) is shown as solid line in Fig. 2. The strong variation of the ratio with Q^2 and x_{Bj} is due to the Q^2 dependence of the trigger efficiency. The average value of the ratio in the kinematic region (2) is 0.67 ± 0.01.

By comparing the initially generated with the reconstructed Monte Carlo events corrections are determined, which are then applied to the data. These corrections include in particular the corrections for radiative effects, reconstruction inefficiencies, measurement errors, particle misidentification, acceptance losses, trigger inefficiencies and the corrections for effects due to secondary interactions, decays and photon conversions in the target.

In the case of the normalized distributions of y^* (see eqs. (19) and (20)), the data are corrected by multiplying the experimental distribution bin-by-bin with a multiplicative correction factor, determined from the event samples of generated and reconstructed Monte Carlo events:

$$\left(\frac{1}{N_{ev}}\frac{dN^h}{dy^*}\right)_{corrected} = \frac{\left(\frac{1}{N_{ev}}\frac{dN^h}{dy^*}\right)^{MC}_{generated}}{\left(\frac{1}{N_{ev}}\frac{dN^h}{dy^*}\right)^{MC}_{reconstructed}} \left(\frac{1}{N_{ev}}\frac{dN^h}{dy^*}\right)_{measured} . \tag{3}$$

This method of correcting the data will be referred to as 'method B' in the following. The distributions of p_T^2 are corrected in the same way.

In the case of the multiplicity distributions of charged hadrons the data are not directly corrected. Instead a theoretical distribution $T(n;\vec{a})$, representing the corrected multiplicity distribution for the ideal non-radiative deep-inelastic interaction ('unsmeared distribution'), is transformed into a reconstructed distribution ('smeared distribution')

$$P_{rec}(m;\vec{a}) = \sum_n C_{mn}\,\varepsilon_n\,T(n;\vec{a}) , \tag{4}$$

which is then compared with the measured multiplicity distribution $P_{meas}(m)$. The parameters $\vec{a}$ of $T(n;\vec{a})$ are determined by minimizing the quantity

$$\chi^2 = \sum_m \frac{(P_{meas}(m) - P_{rec}(m;\vec{a}))^2}{\sigma_m^2} . \tag{5}$$

The matrix C_{mn}, describing the migration from a true multiplicity n to a reconstructed multiplicity m, is obtained by MC calculations. Clearly, only reconstructed MC events can be used to determine the matrix. The factor ε_n corrects for the events which were not reconstructed, due to trigger or reconstruction inefficiencies, and for the events which fall outside the considered kinematic region, due to measurement errors and radiative effects. σ_m^2 is the sum in quadrature of the error of $P_{meas}(m)$ and the error of $\sum_n C_{mn}\,\varepsilon_n\,T(n;\vec{a})$ (due to the errors of C_{mn} and ε_n). This method of obtaining a corrected distribution is called 'method A' in the following.

It should be noted that in this procedure, a corrected multiplicity distribution is not determined. Rather a parametrization of the corrected multiplicity distribution is directly fitted to the data. In this way fluctuations of the corrected multiplicity distribution are avoided, which are inherent in unfolding procedures [19]. The parametrizations $T(n;\vec{a})$ used in the analysis are listed in Sect. 5.1.

Another important feature of the correction method (5) is the fact that the migration matrix C_{mn} depends only weakly on the generated multiplicity distribution. It is essentially determined by the experimental inefficiencies, which are well simulated by the Monte Carlo program. For this reason it is justified to extrapolate C_{mn} to values of n which were not generated in the Monte Carlo program. This was necessary for the correction of the μXe data because the Monte Carlo program did not include nuclear effects, and thus did not generate the high multiplicities which are present in the data. For fixed n the matrix elements C_{mn} can be well approximated by a Gaussian $G(m;\bar{m},\sigma) \approx \frac{1}{\sqrt{2\pi}\sigma} \exp\left(-(m-\bar{m})^2/(2\sigma^2)\right)$, and the extrapolation of C_{mn} to higher n was performed by extrapolating $\bar{m}$ and σ of these Gaussians.

The consistency of the two correction methods (3) and (5) was checked by comparing quantities determined by each of the two methods. Examples are average multiplicities, which were obtained from the analysis of multiplicity distributions (method A according to eq. (5)) as well as by integrating the corrected normalized rapidity distributions (method B according to eq. (3)). The two results (see Table 16) agree within $\sim 1\sigma$ of the statistical error in the D data, and within $\sim 2\sigma$ in the Xe data. For multiplicities, method A is the recommended correction procedure, whereas method B is considered as a check.

5 Theoretical concepts

5.1 Parametrizations of the multiplicity distributions

The analysis of multiplicity distributions (see Sects. 4 and 6) is performed using the negative binomial parametrization [20]

$$P(n;\bar{n},k) = \alpha \binom{n+k-1}{n} \cdot \left(\frac{\bar{n}}{\bar{n}+k}\right)^n \cdot \left(\frac{k}{\bar{n}+k}\right)^k , \tag{6}$$

with the parameters $\bar{n}$ and k. $\bar{n}$ is the average multiplicity, and k (together with $\bar{n}$) determines the dispersion of n: $D^{NBD} = \sqrt{\bar{n} + \frac{\bar{n}^2}{k}}$. In addition, when studying the distributions of the scaled multiplicity $z = \frac{n}{\bar{n}}$, also the Levy and the log-normal functions are considered. The Levy function [21] is defined as

$$P(n;\bar{n},c_{Levy}) = \alpha \frac{c_{Levy}^{(c_{Levy}z+1)}}{\Gamma(c_{Levy}z+1)} e^{-c_{Levy}} , \tag{7}$$

with the parameters $\bar{n}$ and c_{Levy} and the dispersion $D^{Levy} = \bar{n}/\sqrt{c_{Levy}}$. The log-normal function [22] is given by

$$P(n;\bar{n},c_{log},\sigma) = \frac{\alpha}{\sqrt{2\pi}\sigma} \cdot \frac{1}{z+c_{log}} \cdot \exp\left(-\frac{(\ln(z+c_{log})-\mu)^2}{2\sigma^2}\right) , \tag{8}$$

with the parameters $\bar{n}$, c_{log} and σ and the dispersion
$D^{log} = \bar{n}\sqrt{\exp(\sigma^2) - 1} \cdot \exp\left(\mu + \frac{\sigma^2}{2}\right)$. Note that μ is related to c_{log} and σ by the condition that the average value of z has to be 1 [23]. In the expressions (6), (7), and (8), α is a normalisation factor.

5.2 Projectile and cascade interactions

In many models of interactions of particles with nuclei the interaction is interpreted as a sequence of independent collisions of the incident particle or its constituents (henceforth denoted as projectile) with single nucleons inside the nucleus [24]. The products of each projectile interaction may collide with other nucleons of the nucleus and produce more particles. This process is called intra-nuclear cascading [25, 11].

A frequently used measure of the average number of projectile collisions, for interactions on a nucleus with mass number A, is given by [26, 27, 28]

$$\langle \nu_{proj} \rangle = \frac{A\sigma_{aN}}{\sigma_{aA}} . \tag{9}$$

a denotes the projectile (which in the case of muon-nucleus scattering is the virtual photon), and σ_{aN} (σ_{aA}) is the cross section for inelastic collisions with a nucleon (the nucleus). According to (9) multiple projectile collisions ($\nu_{proj} > 1$) are expected when the projectile-nucleus cross section is shadowed. Significant shadowing in the μXe cross section has indeed been observed in the E665 experiment for $x_{Bj} \lesssim 0.02$ [29, 30], however in the data sample of the present analysis, with $\langle x_{Bj} \rangle \approx 0.035$ (see (2) and Table 3), the amount of data in the shadowing region is small. $\langle \nu_{proj} \rangle$, calculated with (9) as a function of x_{Bj} and averaged over the data sample, is found to be 1.09 ± 0.04 (stat.) ± 0.06 (syst.) ± 0.11 (overall syst.).

Whenever a proton is struck, either in the projectile collision or in the cascade process, the total hadronic charge Q_T of the secondary particles increases by 1. Since the fraction of protons in a nucleus is Z/A, and assuming identical cross sections for interactions with protons and neutrons, one obtains the following relation between $\langle Q_T \rangle$ and the total number ν_C of collisions with nucleons in the nucleus [31, 32, 25]:

$$\langle Q_T \rangle = \frac{Z}{A}\langle \nu_C \rangle + \text{charge of projectile}. \tag{10}$$

5.3 The Monte Carlo model VENUS

The Monte Carlo model VENUS (Very Energetic NUclear Scattering) describes hadron production in reactions on nuclei by the interaction of strings in nuclear matter [33]. The model is based on the Dual-Parton model [34] and the Quark-Gluon-String model [35]. Earlier versions of the model dealt with hadron-nucleus and nucleus-nucleus interactions [36]. By the extension to lepton-nucleus scattering [37, 38] the propagation of strings in nuclear matter may be studied for the case of a simple structureless projectile, which interacts only once in the nucleus due to its very small cross section.

QCD effects are not included in the model. The Monte Carlo program version used in the present analysis is VENUS 4.10.

In the initial interaction of the lepton with a nucleon of the nucleus a string consisting of a (anti-)quark and a target remnant is produced. This string may decay into further strings with a typical life time τ_d, which is set to 1 fm. A string may interact (fuse) with another string or with a nucleon, forming a meson or a baryon. This so-called cascade mechanism is steered by several parameters:

- τ_r: a string or a string segment are not allowed to interact before a time τ, where τ is obtained from an exponential distribution with $\langle\tau\rangle = \tau_r$.

- m_r: only strings with a mass below $m_{\min} + m_r$ may interact, where $m_{\min}$ is the minimum mass possible for an object with the right flavor.

- r_B, r_M: when the above conditions are fulfilled, two strings or a string and a nucleon will interact whenever their distance in space-time is below r_B (if a baryon is formed) or below r_M (if a meson is formed).

The default values of these parameters and the values used for the comparisons with the data of the present analysis are listed in Table 4.

6 Results

6.1 Multiplicity distributions of charged hadrons

a) Multiplicity distributions of all charged hadrons

The raw multiplicity distributions in bins of W are shown in Figs. 3 and 4 for μD and μXe scattering respectively. The fitted theoretical distributions, assuming a negative binomial parametrization, are shown as solid lines (unsmeared theoretical distribution $P(n;\bar{n},k)$) and as histograms (smeared theoretical distribution $P_{rec}(m;\bar{n},k)$). In all cases the smeared theoretical distribution describes the raw multiplicity distribution very well. On average, the overall correction for the total average multiplicity is about 10%, due to the migration matrix C_{mn}, and about 5%, due to the factor ε_n (eq. (4)), which includes radiative corrections. In the fits the multiplicity $n = 0$ was not considered, since events with no charged-hadron track in the streamer chamber were not always measured. No good fit was obtained for the highest-W bin in μXe scattering. The enhanced low multiplicities in this W bin, probably due to residual radiative background, cannot be well described by a negative binomial function.

The parameters $\bar{n}$ and $1/k$ of the negative binomial function, obtained in the fits to the multiplicity distributions, are listed in Tables 5 and 6 and displayed as functions of W^2 in Figs. 5 and 6 respectively. The data for both $\bar{n}$ and $1/k$ can be well described

by straight lines of the form $a + b \cdot \ln(W^2/\mathrm{GeV}^2)$, and the fitted parameter values are listed in Tables 7 and 8. The comparisons with predictions from the Monte Carlo model VENUS, which are also shown in Fig. 5, are discussed at the end of Sect. 6.2.

The values of $\bar{n}$ and $1/k$ for μXe are clearly higher than those for μD scattering, the difference being rather independent of W (Figs. 5 and 6). The excess in charged multiplicity, which in the W range 8 to 30 GeV amounts to 2.69 ± 0.20 on the average (Table 9), is attributed to intranuclear cascading of hadrons produced in the initial muon-nucleon interaction.

In Fig. 7 the results for $\bar{n}$ are compared with those from (anti-)neutrino nucleon [39, 40] and muon proton [1] experiments. For simplicity the results from the neutrino-nucleon experiment of ref. [41], which are similar to those of ref. [40], are not plotted. The μD data from the present experiment continue smoothly the trend of the data seen at lower W, however the increase with $\ln(W^2/\mathrm{GeV}^2)$ is steeper in the μD than in the neutrino data (Table 7).

$\bar{n}$ appears to be higher for the μD than for the μp data of the NA9 experiment (Fig. 7), although the systematic errors of the two experiments are large: for the μD data the systematic error of $\bar{n}$ is 0.43 (see Sect. 3.2) and a similar value was quoted for the μp data [42]. A slightly higher average multiplicity is expected in μD scattering due to cascading of hadrons in the deuteron. However, from an (anti-)neutrino deuterium experiment the increase in average charged multiplicity due to this process is estimated to be only of the order 0.1 [43, 44]. The discrepancy in $\bar{n}$ between the μp [1] and the μD data is found to be completely restricted to the forward hemisphere of the hadronic center-of-mass system (see Fig. 15).

The comparison of $1/k$ for the different experiments is shown in Fig. 8. The pattern is similar to that in Fig. 7, with the μD data continuing to higher W the trend of the data seen at lower W. The data suggest a change of sign for $1/k$ at $W^2 \approx 100$–200 GeV^2. The multiplicity distributions are thus narrower than a Poissonian below and broader above this value.

In the comparison of the different lepton-nucleon experiments one has to note that the target remnants have a different composition in the different reactions and in addition depend on the x_{Bj} range covered. It is therefore more informative to compare the forward and backward multiplicities separately (see Sect. 6.1.b).

The higher values of $\bar{n}$ and $1/k$ for μXe as compared to μD scattering at fixed W imply a larger dispersion $D = \sqrt{\bar{n} + \frac{\bar{n}^2}{k}}$ in μXe scattering. The dispersion D_z of the scaled multiplicity $z = \frac{n}{\bar{n}}$, calculated as $D_z = D/\bar{n}$, is listed in Tables 5 and 6 and displayed in Fig. 9 as a function of W^2. For both μD and μXe scattering D_z is independent of W with average values $D_z(\mu\mathrm{D}) = 0.41 \pm 0.01$ and $D_z(\mu\mathrm{Xe}) = 0.47 \pm 0.02$. The size of $D_z(\mu\mathrm{D})$ is comparable to that of most of the neutrino-nucleon reactions at lower W (Fig. 10). In contrast to the μD data the neutrino data, which are at lower W, exhibit some W-dependence, probably due to the stronger relative contribution from quasi-elastic and diffractive channels at low W.

The analysis of the distributions of the scaled multiplicity z was also performed using the Levy and the lognormal functions (see Sect. 5.1). The results are very similar

to those for the negative binomial function, both with respect to $\bar{n}$ and to D_z (Table 10).

Comparing D_z^{log} for the various types of reactions (Table 11) shows that D_z^{log} increases with increasing complexity of the reaction:

$$D_z^{log}(e^+e^-) < D_z^{log}(\nu\mathrm{N}), D_z^{log}(\mu\mathrm{N}) < D_z^{log}(\mu\mathrm{Xe}) < D_z^{log}(pp). \qquad (11)$$

b) Multiplicity distributions in the forward and backward cms hemispheres, and for positive and negative hadrons

Figs. 11 and 12 display $\bar{n}$ and $1/k$ as functions of W^2 for charged hadrons travelling into the forward and backward cms hemispheres. It is evident that the difference seen in $\bar{n}$ and $1/k$ between μD and μXe scattering in Figs. 5 and 6 is almost completely restricted to the backward hemisphere. The difference $\bar{n}(\mu\mathrm{Xe}) - \bar{n}(\mu\mathrm{D})$ in the backward hemisphere is approximately independent of W, with an average value of 2.26 ± 0.16 (Table 9).

In the forward region (Fig. 11b) there is no significant difference in the average multiplicities between μD and μXe scattering, when statistical and systematic errors are taken into account (Table 9). In another analysis from this experiment [14] the z-distributions of charged hadrons were studied using data obtained with the E665 forward spectrometer. The kinematic region considered was 100 GeV $< \nu <$ 500 GeV, 0.1 GeV$^2 < Q^2 <$ 100 GeV^2, $0.001 < x_{Bj} < 0.1$, and $z =$ (laboratory hadron energy)$/\nu \gtrsim 0.1$. In that analysis, which is based on 10975 μD and 9059 μXe events, also no significant difference was found between the z-distributions for μD and μXe scattering.

The excess in $\bar{n}$ and the enhanced value of $1/k$ in μXe scattering is mainly due to positive particles, but to a small extent also to negative particles. This can be seen from Figs. 13 and 14, where $\bar{n}$ and $1/k$ is plotted versus W^2 for positive and negative hadrons separately. The difference $\bar{n}(\mu\mathrm{Xe}) - \bar{n}(\mu\mathrm{D})$ for positive and negative hadrons is again independent of W, with average values of 2.25 ± 0.15 and 0.55 ± 0.11 respectively (Table 9).

The average multiplicities of forward and backward hadrons, listed in Tables 12 and 13, as well as of positive and negative hadrons, listed in Tables 14 and 15, do not exactly add up to the total average multiplicities. This is due to the fact that the multiplicity distributions for the various subsamples and for the total sample of tracks were fitted (and corrected) separately and independently.

In Figs. 15 and 16 the results for $\bar{n}$ and $1/k$ in μD scattering are compared with those in (anti-)neutrino nucleon [40, 47] and muon proton scattering [1], separately for the backward and forward region. The μD data continue the trend of the neutrino data, namely an increase of $\bar{n}$ and $1/k$ with increasing W, to higher energy. In the forward region the mean charged multiplicities (at fixed W) in the different reactions are quite consistent (the differences in $\bar{n}$ between μp from [1] and μD from this experiment are discussed in Sect. 6.1.a). This is to be expected since the forward region is dominated by the fragmentation of $u, d, \bar{u}$ and $\bar{d}$ quarks into pions. Due to isospin and

charge conjugation invariance each of these quark types leads to the same charged-pion multiplicity. There is a larger spread of the data in the backward region, partly due to the different composition of the target remnant in the various reactions. The backward multiplicities in the (anti-)neutrino experiments appear to be ordered according to the total hadronic charge in the various reactions. It is interesting to see that an average of νn and $\bar{\nu} p$ (total hadronic charges 1 and 0) or νp and $\bar{\nu} n$ (total hadronic charges 2 and -1) multiplicities flows smoothly into the higher-energy μD data, which contain an equal mixture of hadronic states with charge 1 (from μp) and charge 0 (from μn scattering).

c) Average hadronic net charge

The average hadronic net charge $\langle Q \rangle$, calculated as the difference between $\bar{n}$ for positive and negative hadrons, is shown as a function of W^2 for the forward and backward hemispheres in Fig. 17. In all cases $\langle Q \rangle$ is independent of W within the experimental errors. Similar to the behaviour in Fig. 11, a significant difference between μD and μXe scattering is only seen in the backward hemisphere. The excess in the average hadronic backward charge $\langle Q_B \rangle_{\mu \mathrm{Xe}}$ of 1.48 ± 0.16 is due to an excess of positive hadrons of 1.87 ± 0.12 and an excess of negative hadrons of 0.39 ± 0.12 in the μXe data. In the forward hemisphere the excess in $\langle Q_F \rangle_{\mu \mathrm{Xe}}$ amounts to 0.16 ± 0.09, resulting from an excess of positive hadrons of 0.23 ± 0.07 and an excess of negative hadrons of 0.07 ± 0.07 in the μXe data (see Table 9).

The average hadronic forward charge for μD and μXe scattering is in good agreement with the prediction of the quark-parton model. This is shown by the dotted line in Fig. 17b, which has been calculated from

$$\langle Q_F \rangle_{QPM}(x_{Bj}) = \frac{\Sigma (e_j - e_{\langle q \rangle}) e_j^2 \, q_j(x_{Bj})}{\Sigma e_j^2 \, q_j(x_{Bj})} \tag{12}$$

for the average x_{Bj} in each W bin. The sums in (12) extend over the various quarks and antiquarks q_j, with charge e_j and distribution function $q_j(x_{Bj})$, in the nucleon. $e_{\langle q \rangle}$ is the charge leakage term [48], which is $\approx +0.07$ (-0.07) for a fragmenting quark (antiquark). For $q_j(x_{Bj})$ the parametrization from [49] was used. Due to the low values of x_{Bj} ($\langle x_{Bj} \rangle = 0.035$) the bulk of the interactions occur on sea quarks. This explains the rather low value of $\langle Q_F \rangle_{QPM}$, since the contributions from sea quarks in the numerator of (12) cancel.

From the average total hadronic net charge the average total number of collisions $\langle \nu_C \rangle$ with nucleons in the nucleus may be derived according to (10). In μXe scattering $\langle \nu_C \rangle$ is found to be 5.37 ± 0.41, while it is compatible with 1.0 in μD scattering (see Table 16). From the data of a neutrino-deuterium experiment [43, 44] a value of $\langle \nu_C \rangle_{\mu \mathrm{D}} \approx 1.10$ is suggested, which is consistent with the measured value of 1.02 ± 0.12 in the present analysis. Assuming the multiplicity excess in the μXe data to be completely due to cascade interactions ($\langle \nu_{cas} \rangle = \langle \nu_C \rangle - 1$), one finds an average multiplicity increase per cascade interaction of

$$\Delta \bar{n} / \langle \nu_{cas} \rangle \;=\; 0.62 \pm 0.07 \tag{13}$$

$$\Delta\bar{n}^{+}/\langle\nu_{cas}\rangle = 0.51 \pm 0.06 \quad (14)$$

$$\Delta\bar{n}^{-}/\langle\nu_{cas}\rangle = 0.13 \pm 0.03\,. \quad (15)$$

The average multiplicities and hadronic net charges, obtained from the analysis of the multiplicity distributions, are compiled in Table 16 (method A). For comparison also the results from the analysis of the rapidity distributions (method B) are included (see Sect. 6.2).

d) Forward-backward multiplicity correlations

The correlation between forward (n_F) and backward (n_B) multiplicities is usually measured by the slope parameter d in the expression

$$\langle n_B \rangle = c + d \cdot n_F\ . \quad (16)$$

When data from different W are combined, the forward-backward multiplicity correlation will contain a contribution due to the increase of $\langle n_B \rangle$ and $\langle n_F \rangle$ with increasing W (Fig. 11). In order to avoid this contribution, the relation (16) has to be investigated at fixed W.

Fig. 18 shows $\langle n_B \rangle$ as a function of n_F in μD scattering, for different bins of W. n_F and n_B were obtained by a track count and the resulting data on $\langle n_B \rangle$ versus n_F were then corrected using a multiplicative correction factor (see Sect. 4). The lines represent the results of fits of expression (16) to the data and the fitted values of d are listed in Table 17. The correlation parameter d tends to be positive and to increase with increasing W, however, the statistical significance of this behaviour is only weak. A similar trend was observed in a μp experiment [42] which covers the W-range up to 20 GeV (see Table 17).

For reasons of limited statistics the forward-backward multiplicity correlation in μXe scattering is measured only in two W bins. Within the experimental errors the values of d for μD and μXe scattering agree, if the same binning in W is chosen (see Fig. 19 and Table 17).

In Fig. 20 $\langle n_B \rangle$ is plotted versus n_F for two selections in the cms-rapidity: $|y^*| < 1.0$ and $|y^*| > 1.0$. While there is a clear correlation in the central rapidity region, the data are consistent with no correlation in the outer y^* regions. This shows that the forward-backward correlation, for both μD and μXe scattering, is of short-range nature. For μD scattering d was also determined for finer bins in W, leading to the same conclusions (see Table 18).

The forward-backward multiplicity correlations in μD interactions were also measured for different charge combinations. No correlation was found between hadrons of equal charge, while a substantial correlation was observed for opposite charges (e.g. $d = 0.05 \pm 0.03$ for $(--)$ and $d = 0.22 \pm 0.04$ for $(+-)$ combinations, with $|y^*| < 1$ and $20 < W < 30$ GeV). This behaviour may be understood as a consequence of the local charge compensation in the hadronization process.

Under the assumption that the forward-backward partition of particles is random and no further forward-backward correlations exist from conservation laws or dynamics,

the correlation parameter d is directly related to the parameter $1/k$ of the negative binomial function for the full multiplicity distribution [50, 51]:

$$d = \frac{\langle n_B \rangle / k}{1 + \langle n_F \rangle / k} . \tag{17}$$

In Fig. 21 the measured values of d are compared with those obtained with (17) as a function of W. In μD scattering the measured d are close to (although systematically slightly higher than) the calculated ones.

There is a larger discrepancy, however, between measured and calculated d in μXe scattering, indicating that the forward-backward partition of particles is not random. This behaviour is attributed to the additional hadrons from the intranuclear cascade, which are predominantly produced in the backward hemisphere. These additional hadrons do not seem to affect the forward-backward correlation, as can be seen from the similarity of d in μD and μXe scattering (Tables 17 and 18).

6.2 Rapidity distributions

The normalized distributions of the cms-rapidity y^* for positive and negative hadrons,

$$\rho^{\pm}(y^*) = \frac{1}{N_{ev}} \cdot \frac{dN^{\pm}}{dy^*} ,$$

are plotted in Fig. 22 and listed in Tables 19 and 20 for three bins of W. The distributions were corrected for the experimental inefficiencies by applying a multiplicative correction factor, bin-by-bin (see eq. (3)). The rapidity distributions for positive hadrons in μXe scattering have a systematic error due to the use of an incomplete Monte Carlo for the μXe reaction (see Sect. 3.2) and the special particle identification procedure applied (see Sect. 3.1). The size of this systematic error may be estimated from Fig. 23, which shows the corrected rapidity distributions for positive hadrons in μXe scattering for three variants of the particle identification procedure: the systematic error of $\rho^+(y^*)$ is in the order of 10 to 20% in the backward hemisphere.

The data in Fig. 22 confirm the observations made for the average multiplicities in Sect. 6.1 : a large excess of positive hadrons and a small excess of negative hadrons in the backward hemisphere in μXe as compared to μD scattering, and nearly identical distributions for μXe and μD scattering in the forward hemisphere. This is seen even more clearly in Fig. 24, which shows the μXe/μD ratio $R_{\mu Xe}(y^*)$ of the normalized rapidity distributions for positive and negative hadrons. The excess in the backward region sets in at $y^* \approx 0$ and increases with decreasing y^*.

The behaviour of $R_{\mu Xe}$ in the central rapidity region is of great interest because it is the region which is populated by the hadrons produced in the projectile collisions [52, 7]. Thus the value of $R_{\mu Xe} \approx 1$ indicates that the virtual photon interacts only once in the Xe nucleus ($\langle \nu_{proj} \rangle_{\mu Xe} \approx 1$), in accordance with the expectation from (9). This is in contrast to hadron-nucleus scattering, where R_{hA} is greater than one, implying multiple collisions of the projectile. An example is given by the dashed curve in Fig. 24a, where

the ratio $R^-_{p\mathrm{Xe}}$, defined as $\rho^-_{p\mathrm{Xe}}/\rho^-_{p\mathrm{D}}$, is shown for comparison [53]. Ref. [53] actually measured the rapidity distributions for positive $\left(\rho^+_{pp}\right)$ and negative hadrons $\left(\rho^-_{pp}\right)$ in pp scattering rather than $\rho_{p\mathrm{D}}$ in pD scattering. These measurements can be used to estimate ρ^-_{pn} in pn scattering: assuming the backward particles ($y^* < 0$) to be mainly fragments of the target nucleon and the forward particles ($y^* > 0$) to be mainly fragments of the projectile nucleon, the approximate relations $\rho^-_{pn} \approx \rho^+_{pp}$ for $y^* < 0$ and $\rho^-_{pn} \approx \rho^-_{pp}$ for $y^* > 0$ follow from isospin symmetry. $\rho^-_{p\mathrm{D}} = \frac{1}{2}\left(\rho^-_{pp} + \rho^-_{pn}\right)$ was therefore approximated by $\frac{1}{2}\left(\rho^-_{pp} + \rho^+_{pp}\right)$ if $y^* < 0$ and by ρ^-_{pp} otherwise. The center-of-mass energy of the proton-nucleon system is 19.4 GeV and thus comparable to the average W of the μD and μXe data ($\langle W \rangle = 17.2$ GeV). In the central rapidity region $R^-_{p\mathrm{Xe}}$ is of the order 2 (Fig. 24a), which is attributed to multiple collisions of the proton in the Xe nucleus [54].

The rapidity distributions of the hadronic net charge for μXe and μD scattering are compared in Fig. 25. The influence of the hadron cascade in the Xe nucleus is again clearly seen in the backward hemisphere, where the hadronic net charge for μXe exceeds that for μD scattering in total by 1.41 ± 0.11 (Table 16). (From the analysis of the multiplicity distributions this quantity was determined as (1.48±0.16) (Table 9), in good agreement with the result obtained here from the analysis of the rapidity distributions.)

Since $\langle \nu_{proj} \rangle_{\mu\mathrm{Xe}} \approx 1$, the spectrum of the charged hadrons produced in the cascade process can be determined as $\rho_{\mu\mathrm{Xe}} - \rho_{\mu\mathrm{D}}$. This quantity is plotted in Fig. 26 for positive and negative hadrons.

The predictions of the Monte Carlo model VENUS (see Sect. 5.3) are drawn as lines in Figs. 5, 22, 24, 25 and 26. The model describes only the gross qualitative features of the data: it predicts the enhanced production of mainly positive hadrons in the backward hemisphere in the μXe reaction, however it is not able to reproduce the shapes of the rapidity distributions, neither in the μD nor in the μXe data. The W dependence of the integrated multiplicities is approximately reproduced by the model (Fig. 5). By a variation of the parameters τ_r, r_B and r_M of the VENUS model it was not possible to significantly improve the agreement between model and data. Further comparisons with the VENUS model are made in Sect. 6.4.

6.3 Transverse momentum distributions

The data for the normalized p_T^2 distributions were corrected in the same way as those for the normalized rapidity distributions, i.e. by a bin-by-bin multiplicative correction factor (see Sect. 4).

The ratio $R^-_{\mu\mathrm{Xe}}(p_T^2)$ of the normalized p_T^2 distributions of negative hadrons from μXe and μD interactions is displayed in Fig. 27 for the forward and backward hemispheres. From the discussion in the previous sections it is clear that most of the hadrons produced in the cascade interactions are emitted into the backward hemisphere. From Fig. 27a one can therefore conclude that the deviation of the ratio $R^-_{\mu\mathrm{Xe}}(p_T^2)$ from 1 is due to hadrons from cascade interactions and that these hadrons have predominantly

low p_T^2. In the forward region on the other hand, there is no significant difference between the p_T^2 distributions for μXe and μD scattering, with the exception of the region around 0.4 $(\mathrm{GeV/c})^2$, where one observes a slight depletion of hadrons in the μXe reaction. A similar result was found in μCu interactions by the EMC collaboration [5].

6.4 Two-particle rapidity correlations

The correlation function for two hadrons h_1^a and h_2^b, with rapidities y_1^* and y_2^* and charges a and b, is defined as

$$R^{ab}\left(y_1^*, y_2^*\right) = \frac{\rho^{ab}\left(y_1^*, y_2^*\right)}{\rho^a\left(y_1^*\right)\rho^b\left(y_2^*\right)} - 1\,, \tag{18}$$

where

$$\rho^a\left(y_1^*\right) = \frac{1}{N_{ev}}\frac{dN_{h_1}^a}{dy_1^*}, \quad \rho^b\left(y_2^*\right) = \frac{1}{N_{ev}}\frac{dN_{h_2}^b}{dy_2^*} \quad \text{and} \tag{19}$$

$$\rho^{ab}\left(y_1^*, y_2^*\right) = \frac{1}{N_{ev}}\frac{dN_{h_1,h_2}^{ab}}{dy_1^*\,dy_2^*} \tag{20}$$

are the normalized 1- and 2-particle rapidity densities. Correlations between particles with similar rapidities ($|\Delta y^*| \lesssim 2$) are usually called short-range correlations (SRC), those with very different rapidities long-range correlations (LRC).

R^{ab} was corrected for the experimental inefficiencies by applying multiplicative correction factors f_{ab}, f_a, f_b to the measurements of ρ^{ab}, ρ^a and ρ^b respectively. The correction factor $f = f_{ab}/(f_a \cdot f_b)$ for the quantity $\rho^{ab}/(\rho^a \cdot \rho^b)$ is plotted as a funtion of y_1^* and y_2^* in Fig. 28. It can be seen that the correction is only important if both y_1^* and y_2^* are below -1. In the remaining part of the (y_1^*, y_2^*) plane f is close to 1, indicating that the corrections to ρ^{ab} and $(\rho^a \cdot \rho^b)$ largely cancel.

The correlation function defined in (18) includes effects due to the dispersion of the hadron multiplicity in the event sample [55]. In order to reduce this contribution, event samples with charged multiplicities between 6 and 10 only are considered. Furthermore, since the results for the whole W-region were found to be qualitatively similar to those for subintervals of W, the data from the whole W-region are combined.

In Fig. 29 the corrected correlation function $R^{++}\left(y_1^*, y_2^*\right)$ for two positive hadrons (h_1^+, h_2^+) is shown as a function of y_2^* for different bins of y_1^* (the hadron h_1 plays the role of a 'trigger' particle). The correlation function $R^{+-}(y_1^*, y_2^*)$ for hadrons of opposite charge (h_1^+, h_2^-) is displayed in Fig. 30. The correlation function $R^{--}(y_1^*, y_2^*)$ for pairs of negative hadrons is not shown as it is very similar in μD and μXe scattering and, in addition, $R_{\mu\mathrm{D}}^{--}(y_1^*, y_2^*) \approx R_{\mu\mathrm{D}}^{++}(y_1^*, y_2^*)$.

Consider first the μD data (full circles). Between positive hadrons, there are anti-correlations of short range ($|\Delta y^*| \lesssim 2-3$), when the trigger particle is near the lower end of the rapidity range. Between hadrons of opposite charge there are significant SRCs in the central rapidity region. There are indications of positive LRCs between particles at the opposite edges of the rapidity range. In general $R^{ab}\left(y_1^*, y_2^*\right)$ is different from $R^{ab}\left(-y_1^*, -y_2^*\right)$, i.e. the correlation function is not forward-backward symmetric.

The correlations in the μD data are in general well described by the VENUS model (dotted lines in Figs. 29 and 30) and can thus to a large extent be understood in the framework of the quark-parton model. The positive SRCs between particles of opposite charge suggest local charge compensation in the fragmentation process; partly they can be explained by resonance decays [56]. The LRCs may be partly due to momentum conservation. The forward-backward asymmetry is not surprising since the objects emitted into the forward hemisphere (struck quark) and into the backward hemisphere (target remnant) are of different nature.

The correlations in the μXe (open circles) data are similar to those in the μD data. A clear difference is only seen for SRCs between positive hadrons in the backward region: the anticorrelations in the μD data have nearly disappeared in the μXe data.

The VENUS model (lines in Figs. 29 and 30) is able to describe the behaviour of the correlations in the μXe data qualitatively. This supports the concept of cascading in a nucleus. The cascade interactions destroy the negative SRCs between positive particles in the low-rapidity region.

7 Summary

This analysis extends the measurements on hadron production in deep-inelastic muon-nucleon scattering from previous experiments into a region of higher W, up to $W = 30$ GeV. It represents the first study of the complete system of charged hadrons in muon interactions on a heavy nucleus. The results may be summarized as follows.

a) The multiplicity distributions of charged hadrons for both μD and μXe scattering are well described by negative binomial functions. The average multiplicity $\bar{n}$ and the parameter $1/k$ of the negative binomial function increase approximately linearly with $\ln(W^2/\mathrm{GeV}^2)$. The width of the distribution of the scaled multiplicity $z = n/\bar{n}$ is independent of W.

b) The average multiplicity of forward and backward going charged hadrons, as well as of positive and negative hadrons, for both μD and μXe scattering, also exhibit a linear increase with $\ln(W^2/\mathrm{GeV}^2)$. The same is true for the parameter $1/k$, except for the hadrons in the backward region, where $1/k$ is independent of W.

c) The average hadronic forward charge $\langle Q_F \rangle$ and the average hadronic backward charge $\langle Q_B \rangle$ for both μD and μXe scattering are consistent with being independent of W.

d) In the W range 8 – 30 GeV the average multiplicity of charged hadrons in μXe is greater than that in μD scattering by 2.69 ± 0.20 charged hadrons per event, rather independent of W. The excess is mainly due to positive particles in the backward direction and it is attributed to cascade interactions of the hadrons produced in the initial muon-nucleon interaction.

e) The Xe/D ratio $R_{\mu\mathrm{Xe}}(y^*)$ of the average charged multiplicity is compatible with 1 in the forward region of the hadronic center-of-mass system. In the backward

region the ratio rises with decreasing cms-rapidity and with decreasing p_T^2. From the value $R_{\mu Xe}(y^*) \approx 1$ in the central rapidity region it is concluded that the virtual photon interacts only once in the Xe nucleus. This is in contrast to hadron-nucleus reactions, where an enhanced hadron production is observed also in the central rapidity region, which is explained by multiple projectile collisions.

f) From the average hadronic net charge $\langle Q_T \rangle_{\mu Xe}$ the average total number of collisions with nucleons in the Xe nucleus is found to be 5.37 ± 0.41. Assuming that the virtual photon interacts only with one nucleon in the Xe nucleus, this implies an average multiplicity increase per cascade interaction of 0.51 ± 0.06 positive and 0.13 ± 0.03 negative hadrons.

g) The correlation between the average backward multiplicity and the forward multiplicity tends to be positive and to increase with increasing hadronic mass W, for both μD and μXe scattering. The correlation is of short-range nature and it is only significant for $|y^*| < 1$. The μXe data are clearly inconsistent with random forward-backward partitioning of particles. This behaviour is attributed to the additional hadrons in the backward region from the intranuclear cascade.

h) There are short-range and indications of long-range two-particle rapidity correlations in the μD data. They can be understood in the framework of the quark-parton model, and as a consequence of resonance production, local charge compensation in quark fragmentation and of momentum conservation. In general, the two-particle rapidity correlations in the μXe are similar to those in the μD data. There is a clear difference in the SRCs between positive particles in the backward region: they are negative for μD and have nearly disappeared in μXe scattering, as a result of the cascade interactions in the Xe nucleus.

i) The Monte Carlo model VENUS is able to describe the gross qualitative features of the data, in particular those related to the cascading of hadrons in the Xe nucleus.

Acknowledgements

We wish to thank all those persons, both at Fermilab and the participating institutions, who have contributed to the success of this experiment. We thank B. Leupold, P. Strube and M. Vidal for their excellent work in the production and processing of the streamer chamber data. We are grateful to B. Kopeliovich and N. Nikolaev for many fruitful and enlightening discussions.

This work was performed at the Fermi National Accelerator Laboratory, which is operated by Universities Research Association, Inc., under contract DE-AC02-76CHO3000 with the U.S. Department of Energy. The work of the University of California, San Diego was supported in part by the National Science Foundation, contract numbers PHY82-05900, PHY85-11584, and PHY88-10221; the University of Illinois at Chicago by NSF contract PHY88-11164; and the University of Washington by NSF contract

numbers PHY83-13347 and PHY86-13003. The University of Washington was also supported by the U.S. Department of Energy. The work of Argonne National Laboratory was supported by the Department of Energy, Nuclear Physics Division, under Contract No. W-31-109-ENG-38. The Department of Energy, High Energy Physics Division, supported the work of Harvard University, the University of Maryland, the Massachussetts Institute of Technology under Contract No. DE-AC02-76ER03069, Northwestern University under Contract No. DE-FG02-91ER40684, and Yale University. The Albert-Ludwigs-Universität Freiburg and the University of Wuppertal were supported in part by the Bundesministerium für Forschung und Technologie. The work of the Institute for Nuclear Physics, Krakow, was supported in part by the Polish Committee for Scientific Research.

References

[1] M. Arneodo et al., Z. Phys. **C35** (1987) 335

[2] N. Schmitz, Int. J. Mod. Phys. **A3**, No.9 (1988) 1997

[3] J. Ashman et al., Z. Phys. **C52** (1991) 361

[4] A. Arvidson et al., Nucl. Phys. **B246** (1984) 381

[5] J. Ashman et al., Z. Phys. **C52** (1991) 1;
N. Pavel, Ph.D. Thesis, University of Wuppertal, WUB 89-24 (1989)

[6] A. Salvarani, Ph.D. Thesis, University of California, San Diego (1991)

[7] A. Białas, 13th Intern. Symp. on Multiparticle Dynamics, Volendam, The Netherlands (1982) 328, eds. W. Kittel et al., World Scientific, Singapore 1983

[8] J.D. Bjorken, SLAC-PUB-1756 (1975)

[9] G.V. Davidenko, N.N. Nikolaev, Nucl. Phys. **B135** (1978) 333

[10] A. Białas, W. Czyz, Nucl. Phys. **B137** (1978) 359

[11] L. Hand et al., Acta Phys. Pol. **B9** (1978) 1087

[12] M. R. Adams et al., Nucl. Inst. and Meth., **A291** (1990) 533

[13] S. Söldner-Rembold, Ph.D. Thesis, Technische Universität München (1992), MPI report MPI-PhE/92-17 (October 1992)

[14] M.R. Adams et al., Scaled Energy (z) Distributions of Charged Hadrons Observed in Deep-Inelastic Muon Scattering at 490 GeV from Xenon and Deuterium Targets, paper submitted to Phys. Rev. **D** (1993)

[15] T. Sjöstrand, Comput. Phys. Commun. **27** (1982) 243;
T. Sjöstrand, Comput. Phys. Commun. **39** (1986) 347

[16] N. Pavel, Internal EMC report, EMC/88/2 (1988)

[17] L. W. Mo,Y. S. Tsai, Rev. Mod. Phys. **41** (1969) 205

[18] R. Brun et al., GEANT 3, CERN DD/EE/84–1 (1987)

[19] V. Blobel, DESY 84–118 (1984)

[20] A. Giovannini, L. Van Hove, Z. Phys. **C30** (1986) 391;
L. Van Hove, A. Giovannini, Proc. 17th Intern. Symp. on Multiparticle Dynamics, Seewinkel, Austria (1986) 561, eds. M. Markytan et al., World Scientific, Singapore 1987

[21] D. Levy, Nucl. Phys. **B59** (1973) 583

[22] R. Szwed, G. Wrochna, Z. Phys. **C47** (1990) 449;
R. Szwed et al., Mod. Phys. Lett. **A5** (1990) 1851

[23] G. Wrochna, preprint, University Warsaw, IFD/8/1990 (1990)

[24] K. Zalewski, Proc. of the Topical Meeting on Multiparticle Production on Nuclei at Very High Energies, Trieste, Italy (1976) 145, eds. G. Bellini et al., Center for Theoretical Physics, Trieste 1977

[25] A. Dar, J. Vary, Phys. Rev. **D6** (1972) 2412

[26] A. Białas, W. Czyz, Phys. Lett. **B51** (1974) 179

[27] A. Gurtu et al., Pramana **3** (1974) 311

[28] W. Busza et al., Phys. Rev. Lett. **34** (1975) 836

[29] M.R. Adams et al., Phys. Rev. Lett. **69** (1992) 3266

[30] M.R. Adams et al., Phys. Lett. **B287** (1992) 375

[31] F. Roesler, C.B.A. McCusker, Nuovo Cim. **10** (1953) 127

[32] I.Z. Artykov et al., Nucl. Phys. **B6** (1968) 11

[33] K. Werner, HD-TVP-93-1, to be published in Physics Reports

[34] A. Capella et al., Z. Phys. **C33** (1987) 541; Hadronic Multiparticle Production, P. Carruthers ed., Advanced Series on Directions in High Energy Physics, Vol. 2, p. 428 (1988)

[35] A. Kaidolov, Nucl. Phys. **A525** (1991) 390

[36] K. Werner, Phys. Lett. **B208** (1988) 520; K. Werner, Phys. Rev. **D39** (1989) 780; K. Werner, P. Koch, Phys. Lett. **B242** (1990) 251

[37] K. Werner, P. Koch, Z. Phys. **C47** (1990) 255

[38] K. Werner, CERN-TH-5682/90, Cape Town Summer School (1990), p. 133

[39] G. T. Jones et al., Z. Phys. **C54** (1992) 45

[40] B. Jongejans et al., Nuovo Cim. **A101** (1989) 435

[41] D. Zieminska et al., Phys. Rev. **D27** (1983) 47

[42] M. Arneodo et al., Nucl. Phys. **B258** (1985) 249

[43] A. G. Tenner, N.N.Nikolaev, Nuovo Cim. **A105** (1992) 1001

[44] A. Tenner, NIKHEF-H/88-6 (1988)

[45] R. Szwed et al., Mod. Phys. Lett. **A6** (1991) 245

[46] M. Gazdzicki et al., Mod. Phys. Lett. **A6** (1991) 981

[47] D. Allasia et al., Z. Phys. **C24** (1984) 119

[48] R. D. Field, R. P. Feynman, Nucl. Phys. **B136** (1978) 1

[49] M. Glück, E. Hoffmann, E. Reya, Z. Phys. **C13** (1982) 119

[50] P. Carruthers, C.C. Shih, Phys. Lett. **165B** (1985) 209;
W.A. Zajc, Phys. Lett. **B175** (1986) 219; A. Bialas, A. Szczerba, Acta Phys. Pol. **B17** (1986) 1085; **B18** (1987) 681

[51] D. Zieminska, Phys. Rev. **D27** (1983) 502

[52] S.J. Brodsky et al., Phys. Rev. Lett. **39** (1977) 1120

[53] C. De Marzo et al., Phys. Rev. **D26** (1982) 1019

[54] C. De Marzo et al., Phys. Rev. **D29** (1984) 2476

[55] R. Singer et al., Phys. Lett. **B49** (1974) 481

[56] S. Maselli, Ph.D. Thesis, Technische Universität München (1988)

target	A	Z	density [g/cm^3]	length [m]	number of interaction lengths	number of radiation lengths
H_2	1.01	1	0.071	1.15	0.16	0.13
D_2	2.01	1	0.162	1.15	0.34	0.15
Xe	131.29	54	0.085	1.13	0.06	1.13

Table 1: Main parameters of the targets.

source of systematic error	$\Delta\bar{n}$	
	D	Xe
dependence on vertex position	0.35 (4.5%)	—
dependence on measuring lab	0.20 (2.6%)	0.25 (2.4%)
MC-correction	0.10 (1.3%)	0.30 (2.9%)
trigger simulation	0.10 (1.3%)	0.10 (1.0%)
total systematic error	0.43 (5.5%)	0.40 (3.9%)

Table 2: Contributions to the systematic error of the average total multiplicity of charged hadrons. The total systematic error was calculated by adding the various contributions in quadrature. The numbers in brackets are the respective relative errors.

W-interval (GeV)	N_{ev}(D)	N_{ev}(Xe)	$\langle W \rangle$ (GeV)	$\langle x_{Bj} \rangle$	$\langle \nu \rangle$ (GeV)
8–10	472	170	9.3	0.096	51.5
10–12	792	311	11.0	0.065	69.0
12–14	777	284	13.0	0.044	94.0
14–16	732	228	14.9	0.038	124.
16–18	709	202	17.0	0.025	157.
18–20	666	207	19.0	0.021	197.
20–22	695	220	21.0	0.015	238.
22–25	829	280	23.4	0.013	295.
25–30	637	162	26.6	0.009	380.
8–30	6309	2064	17.2	0.035	176.

Table 3: Number of events and average values of W, x_{Bj} and ν in different W-bins. There is only a small decrease of $\langle Q^2 \rangle$ with increasing W, with $\langle Q^2 \rangle \approx 9$ GeV^2 at low and ≈ 7 GeV^2 at high W. The average values were calculated for the D sample. Within the errors they agree with those of the Xe sample.

Symbol	Meaning	Fortran variable	Default value	Value used in this analysis
τ_r	reaction time	taurea	1.5 fm	1.5 fm
m_r	mass cutoff	amsiac	0.8 GeV	0.8 GeV
r_B	baryon radius	radiac	0.65 fm	0.55 fm
r_M	meson radius	radias	0.35 fm	0.35 fm

Table 4: Parameters of the VENUS model, version 4.10.

W (GeV)	$1/k$	$\bar{n}$	D_z	χ^2/NDF
8–10	−0.011±0.026	5.69±0.19	0.41±0.03	5.8/13
10–12	−0.002±0.019	6.47±0.17	0.40±0.02	5.0/11
12–14	0.061±0.021	6.86±0.19	0.45±0.02	8.0/14
14–16	0.033±0.018	7.69±0.21	0.40±0.02	8.2/16
16–18	0.057±0.022	8.00±0.25	0.43±0.03	15.3/21
18–20	0.062±0.025	8.24±0.25	0.43±0.03	19.5/15
20–22	0.041±0.019	8.49±0.23	0.40±0.02	13.6/17
22–25	0.047±0.017	8.87±0.22	0.40±0.02	22.6/18
25–30	0.095±0.032	8.94±0.33	0.46±0.04	22.5/22

Table 5: Results of fits of the negative binomial function to the multiplicity distributions of charged hadrons in μD scattering, in different bins of W. $D_z = \sqrt{\frac{1}{\bar{n}} + \frac{1}{k}}$ is the dispersion of the scaled multiplicity $z = n/\bar{n}$. The fitted functions are drawn as solid lines in Fig. 3.

W (GeV)	$1/k$	$\bar{n}$	D_z	χ^2/NDF
8–10	0.068±0.049	7.92±0.54	0.44±0.06	11.6/17
10–12	0.112±0.035	9.00±0.50	0.47±0.04	8.4/20
12–14	0.146±0.042	9.54±0.45	0.50±0.04	8.5/20
14–16	0.142±0.050	10.42±0.68	0.49±0.05	17.6/21
16–18	0.053±0.036	10.49±0.49	0.38±0.05	9.9/22
18–20	0.142±0.045	11.34±0.61	0.48±0.05	13.7/22
20–22	0.147±0.047	11.02±0.62	0.49±0.05	14.5/19
22–25	0.214±0.066	12.29±0.80	0.54±0.06	21.8/26

Table 6: Results of fits of the negative binomial function to the multiplicity distributions of charged hadrons in μXe scattering, in different bins of W. $D_z = \sqrt{\frac{1}{\bar{n}} + \frac{1}{k}}$ is the dispersion of the scaled multiplicity $z = n/\bar{n}$. The fitted functions are drawn as solid lines in Fig. 4.

reaction	W (GeV)	a	b	χ^2/NDF	reference
μD	8–30	-1.50 ± 0.59	1.64 ± 0.10	4.8/7	this exp.
μXe	8–25	-1.50 ± 1.88	2.16 ± 0.35	1.7/6	this exp.
μp	4–20	-0.19 ± 0.09	1.30 ± 0.01	1.9/6	[1]
νp	3–14	0.40 ± 0.13	1.25 ± 0.04	1.6/3	[39]
$\bar{\nu} p$	3–14	-0.44 ± 0.20	1.30 ± 0.06	2.7/3	[39]

Table 7: Parameter values a and b from fits of the expression $(a + b\ln(W^2/\mathrm{GeV}^2))$ to the average multiplicity $\bar{n}$ of charged hadrons in various lepton-nucleon experiments. The results of the fits to the data of this experiment are drawn as dashed and solid lines in Fig. 5.

reaction	W (GeV)	a	b	χ^2/NDF	reference
μD	8–30	-0.13 ± 0.01	0.030 ± 0.002	6.4/7	this exp.
μXe	8–25	-0.05 ± 0.15	0.031 ± 0.028	6.5/6	this exp.
νp	3–14	-0.187 ± 0.016	0.035 ± 0.005	7.6/3	[39]
$\bar{\nu} p$	3–14	-0.132 ± 0.040	0.027 ± 0.011	1.9/3	[39]

Table 8: Parameter values a and b from fits of the expression $(a + b\ln(W^2/\mathrm{GeV}^2))$ to the experimental data of $1/k$ in various lepton-nucleon experiments. The results of the fits to the data of this experiment are drawn as dashed and solid lines in Fig. 6.

	F+B	B	F
$\Delta\bar{n}^+$	2.25 ± 0.15	1.87 ± 0.12	0.23 ± 0.07
$\Delta\bar{n}^-$	0.55 ± 0.11	0.39 ± 0.12	0.07 ± 0.07
$\Delta\bar{n}$	2.69 ±0.20	2.26 ± 0.16	0.29 ± 0.11
$\Delta\langle Q\rangle$	1.70 ± 0.19	1.48 ± 0.16	0.16 ± 0.09

Table 9: Differences of average charged multiplicities and of average hadronic net charges between μXe and μD scattering in the W range 8–30 GeV. F and B refer to the forward and backward hemispheres of the hadronic center-of-mass system respectively.

reaction	W (GeV)	D_z^{NBD}	D_z^{Levy}	D_z^{log}
μD	8 – 30	0.41±0.01	0.41±0.01	0.41±0.01
μXe	8 – 30	0.47±0.02	0.47±0.02	0.48±0.05

Table 10: Dispersion D_z of the scaled multiplicity $z = n/\bar{n}$ from global fits of the negative binomial function (D_z^{NBD}), the Levy function (D_z^{Levy}) and the lognormal function (D_z^{log}) to the μD and μXe data in the W range $8 < W < 30$ GeV. The results for D_z^{NBD} are drawn as dashed and solid lines in Fig. 9.

reaction	W (GeV)	c_{log}	D_z^{log}	χ^2/NDF	reference
e^+e^-	$7 < \sqrt{s} < 91$	0.56± 0.03	0.277±0.001	208 /285	[45]
νp	$3 < W < 14$	2.41± 0.69	0.470±0.007	26.9/ 18	[39]
$\bar{\nu} p$	$3 < W < 12$	1.37± 0.42	0.357±0.007	8.4/ 18	[39]
μD	$8 < W < 30$	1.86± 0.75	0.41 ±0.01	126.1/154	this exp.
μXe	$8 < W < 30$	13.29± 13.80	0.48 ±0.05	140.1/190	this exp.
pp	$3 < \sqrt{s} < 62$	4.25± 0.20	0.629±0.003	458 /316	[46]

Table 11: Dispersion D_z^{log} of lognormal functions fitted to the distributions of the scaled multiplicity $z = n/\bar{n}$ in various types of reactions.

W (GeV)	backward		forward	
	$1/k$	$\bar{n}$	$1/k$	$\bar{n}$
8-10	0.149 ± 0.092	2.46 ± 0.17	-0.099 ± 0.037	3.32 ± 0.13
10-12	0.144 ± 0.063	2.83 ± 0.14	-0.043 ± 0.030	3.79 ± 0.13
12-14	0.255 ± 0.079	2.68 ± 0.14	0.001 ± 0.028	4.11 ± 0.14
14-16	0.152 ± 0.063	3.18 ± 0.17	-0.038 ± 0.027	4.53 ± 0.14
16-18	0.172 ± 0.078	3.22 ± 0.17	0.058 ± 0.035	4.91 ± 0.20
18-20	0.102 ± 0.084	3.33 ± 0.21	0.019 ± 0.029	4.90 ± 0.18
20-22	0.202 ± 0.070	3.57 ± 0.19	-0.046 ± 0.025	4.86 ± 0.15
22-25	0.163 ± 0.056	3.95 ± 0.17	0.030 ± 0.035	5.06 ± 0.18
25-30	0.205 ± 0.075	3.98 ± 0.22	0.029 ± 0.034	5.27 ± 0.20

Table 12: Results of fits of the negative binomial function to the multiplicity distribution of charged hadrons in μD scattering, for the backward and forward hemispheres of the hadronic cms and in different bins of W.

W (GeV)	backward		forward	
	$1/k$	$\bar{n}$	$1/k$	$\bar{n}$
8-10	0.499 ± 0.161	4.76 ± 0.58	-0.053 ± 0.097	3.37 ± 0.31
10-12	0.413 ± 0.084	5.08 ± 0.37	-0.034 ± 0.058	3.96 ± 0.23
12-14	0.654 ± 0.143	5.28 ± 0.49	-0.021 ± 0.044	4.28 ± 0.22
14-16	0.533 ± 0.144	5.72 ± 0.55	-0.072 ± 0.072	4.67 ± 0.41
16-18	0.214 ± 0.093	6.10 ± 0.43	-0.046 ± 0.064	5.21 ± 0.38
18-20	0.382 ± 0.110	5.82 ± 0.52	0.009 ± 0.050	5.38 ± 0.31
20-22	0.542 ± 0.143	5.91 ± 0.58	0.035 ± 0.062	5.53 ± 0.39
22-25	0.780 ± 0.205	6.69 ± 0.70	0.127 ± 0.062	5.32 ± 0.34

Table 13: Results of fits of the negative binomial function to the multiplicity distribution of charged hadrons in μXe scattering, for the backward and forward hemispheres of the hadronic cms and in different bins of W.

W (GeV)	positive		negative	
	$1/k$	$\bar{n}$	$1/k$	$\bar{n}$
8-10	-0.128 ± 0.040	3.07 ± 0.13	-0.208 ± 0.028	2.58 ± 0.09
10-12	-0.137 ± 0.029	3.47 ± 0.10	-0.178 ± 0.027	2.91 ± 0.08
12-14	-0.055 ± 0.033	3.60 ± 0.13	-0.079 ± 0.027	3.19 ± 0.10
14-16	-0.075 ± 0.029	4.08 ± 0.13	-0.093 ± 0.025	3.58 ± 0.11
16-18	-0.065 ± 0.026	4.27 ± 0.15	-0.029 ± 0.029	3.74 ± 0.14
18-20	-0.057 ± 0.022	4.43 ± 0.14	-0.041 ± 0.031	3.82 ± 0.13
20-22	-0.077 ± 0.021	4.54 ± 0.13	-0.071 ± 0.025	3.97 ± 0.12
22-25	-0.066 ± 0.018	4.81 ± 0.12	-0.050 ± 0.026	4.13 ± 0.12
25-30	-0.052 ± 0.021	4.86 ± 0.15	-0.029 ± 0.029	4.38 ± 0.15

Table 14: Results of fits of the negative binomial function to the multiplicity distribution of positive and negative hadrons in μD scattering, in different bins of W.

W (GeV)	positive		negative	
	$1/k$	$\bar{n}$	$1/k$	$\bar{n}$
8-10	0.047 ± 0.075	5.05 ± 0.41	-0.050 ± 0.076	2.90 ± 0.25
10-12	0.127 ± 0.053	5.56 ± 0.32	-0.046 ± 0.041	3.53 ± 0.18
12-14	0.155 ± 0.062	6.07 ± 0.39	-0.035 ± 0.045	3.62 ± 0.19
14-16	0.134 ± 0.061	6.30 ± 0.42	0.033 ± 0.059	4.15 ± 0.29
16-18	0.015 ± 0.041	6.64 ± 0.36	-0.086 ± 0.040	4.34 ± 0.21
18-20	0.075 ± 0.055	6.62 ± 0.42	-0.016 ± 0.055	4.59 ± 0.26
20-22	0.166 ± 0.074	6.35 ± 0.43	0.018 ± 0.045	4.63 ± 0.27
22-25	0.188 ± 0.069	7.45 ± 0.61	0.131 ± 0.067	4.89 ± 0.32

Table 15: Results of fits of the negative binomial function to the multiplicity distribution of positive and negative hadrons in μXe scattering, in different bins of W.

reaction	quantity	method A	method B
μD	$\bar{n}^+$	4.12±0.04	4.16±0.05
	$\bar{n}^-$	3.61±0.04	3.67±0.05
	$\bar{n}_F$	4.51±0.05	4.60±0.05
	$\bar{n}_B$	3.28±0.05	3.23±0.04
	$\bar{n}$	7.74±0.07	7.83±0.07
	$\langle Q_F \rangle$	0.05±0.04	0.05±0.05
	$\langle Q_B \rangle$	0.45±0.10	0.44±0.04
	$\langle Q_T \rangle$	0.51±0.06	0.49±0.06
	$\langle \nu_C \rangle$	1.02±0.12	0.98±0.12
μXe	$\bar{n}^+$	6.37±0.14	6.00±0.11
	$\bar{n}^-$	4.16±0.10	3.99±0.06
	$\bar{n}_F$	4.80±0.10	4.70±0.07
	$\bar{n}_B$	5.54±0.15	5.29±0.11
	$\bar{n}$	10.43±0.19	9.99±0.13
	$\langle Q_F \rangle$	0.21±0.08	0.15±0.10
	$\langle Q_B \rangle$	1.93±0.13	1.85±0.10
	$\langle Q_T \rangle$	2.21±0.17	2.00±0.14
	$\langle \nu_C \rangle$	5.37±0.41	4.86±0.34

Table 16: Results for the average multiplicity of positive ($\bar{n}^+$), negative ($\bar{n}^-$), forward ($\bar{n}_F$), backward ($\bar{n}_B$) and all charged ($\bar{n}$) hadrons, and for the average hadronic forward ($\langle Q_F \rangle$), backward ($\langle Q_B \rangle$) and total ($\langle Q_T \rangle$) charge. $\langle \nu_C \rangle$ was calculated from $\langle Q_T \rangle$ using eq. (10). Method A: results from the analysis of the multiplicity distributions, method B: results from the analysis of the rapidity distributions (see Sect. 4).

W [GeV]	μD	μD	μXe	μp [42]
4- 8				0.08±0.03
8-12	0.06±0.06			−0.02±0.02
12-16	0.12±0.06	0.09±0.03	0.10±0.08	0.02±0.02
16-20	0.17±0.07			0.05±0.02
20-25	0.19±0.07	0.18±0.05	0.30±0.11	
25-30	0.04±0.12			

Table 17: Fitted values of the parameter d in the expression $\langle n_B \rangle = c + d \cdot n_F$ for μD and μXe scattering from this experiment and for μp scattering [42].

	W [GeV]	$\|y^*\| < 1$	$\|y^*\| > 1$
μD	8-12	0.15±0.05	0.05±0.08
	12-16	0.24±0.05	0.01±0.06
	16-20	0.24±0.06	−0.16±0.07
	20-25	0.22±0.06	0.01±0.07
	25-30	0.35±0.09	−0.09±0.11
	8-20	0.20±0.02	0.05±0.04
	20-30	0.24±0.04	−0.05±0.05
	8-30	0.22±0.02	0.06±0.03
μXe	8-20	0.27±0.04	−0.15±0.10
	20-30	0.35±0.05	0.17±0.14
	8-30	0.29±0.03	0.04±0.08

Table 18: Fitted values of the parameter d in the expression $\langle n_B \rangle = c + d \cdot n_F$ for a central and an outer cms-rapidity region, for μD and μXe scattering in different bins of W.

y^* interval		$8 < W < 14$ GeV		$14 < W < 20$ GeV		$20 < W < 30$ GeV	
		positive	negative	positive	negative	positive	negative
-4.0	-3.5	–	–	–	–	–	0.01±0.01
-3.5	-3.0	–	0.01±0.01	0.03±0.02	0.02±0.01	0.07±0.01	0.03±0.01
-3.0	-2.5	0.04±0.01	0.02±0.01	0.15±0.02	0.06±0.02	0.35±0.04	0.11±0.02
-2.5	-2.0	0.27±0.03	0.09±0.02	0.42±0.04	0.23±0.03	0.56±0.04	0.33±0.03
-2.0	-1.5	0.54±0.05	0.22±0.02	0.62±0.05	0.38±0.03	0.82±0.05	0.57±0.04
-1.5	-1.0	0.61±0.04	0.45±0.03	0.71±0.04	0.58±0.04	0.78±0.04	0.63±0.04
-1.0	-0.5	0.75±0.04	0.60±0.04	0.72±0.04	0.71±0.04	0.79±0.04	0.79±0.05
-0.5	0.	0.81±0.05	0.78±0.05	0.96±0.05	0.85±0.05	0.98±0.05	0.95±0.05
0.	0.5	0.92±0.05	0.85±0.05	1.03±0.06	1.05±0.06	0.94±0.05	0.89±0.05
0.5	1.0	0.97±0.06	0.88±0.06	0.96±0.06	0.97±0.06	1.00±0.06	1.00±0.06
1.0	1.5	0.85±0.06	0.84±0.06	0.99±0.06	0.97±0.07	0.93±0.06	1.08±0.07
1.5	2.0	0.65±0.05	0.83±0.07	0.94±0.07	0.80±0.06	0.93±0.07	0.91±0.06
2.0	2.5	0.39±0.04	0.42±0.05	0.53±0.05	0.54±0.05	0.70±0.06	0.71±0.06
2.5	3.0	0.12±0.02	0.12±0.02	0.26±0.03	0.27±0.03	0.45±0.05	0.35±0.04
3.0	3.5	0.05±0.01	0.02±0.01	0.09±0.02	0.07±0.01	0.20±0.03	0.15±0.02
3.5	4.0	0.01±0.01	0.01±0.01	0.04±0.02	0.01±0.01	0.05±0.01	0.03±0.01
4.0	4.5	–	–	–	–	0.01±0.01	0.01±0.01

Table 19: Normalized cms-rapidity distribution $\rho(y^*)$ for positive and negative hadrons in μD scattering.

y^* interval		$8 < W < 14$ GeV		$14 < W < 20$ GeV		$20 < W < 30$ GeV	
		positive	negative	positive	negative	positive	negative
-4.0	-3.5	–	–	–	0.02±0.02	0.28±0.23	0.01±0.01
-3.5	-3.0	–	0.02±0.01	0.62±0.24	0.02±0.01	0.63±0.10	0.06±0.02
-3.0	-2.5	0.61±0.15	0.05±0.02	0.96±0.11	0.12±0.03	1.02±0.11	0.15±0.03
-2.5	-2.0	1.18±0.12	0.16±0.03	1.38±0.13	0.26±0.04	1.33±0.12	0.41±0.05
-2.0	-1.5	1.38±0.12	0.39±0.05	1.30±0.10	0.60±0.06	1.06±0.08	0.64±0.06
-1.5	-1.0	1.28±0.09	0.65±0.06	1.12±0.08	0.77±0.06	0.96±0.07	0.80±0.06
-1.0	-0.5	1.09±0.07	0.75±0.06	1.11±0.08	0.87±0.07	0.98±0.06	0.86±0.06
-0.5	0.	0.99±0.07	0.88±0.06	1.08±0.07	1.00±0.07	1.01±0.07	1.01±0.07
0.	0.5	0.97±0.07	0.88±0.06	1.11±0.07	1.01±0.07	1.08±0.07	0.99±0.07
0.5	1.0	0.92±0.06	0.88±0.07	1.05±0.08	1.04±0.08	0.99±0.08	0.99±0.08
1.0	1.5	0.81±0.07	0.71±0.06	1.01±0.08	0.94±0.08	1.10±0.09	1.16±0.10
1.5	2.0	0.78±0.07	0.62±0.07	0.99±0.10	0.95±0.09	0.92±0.09	0.90±0.09
2.0	2.5	0.38±0.05	0.30±0.04	0.71±0.08	0.55±0.07	0.67±0.07	0.70±0.07
2.5	3.0	0.14±0.03	0.11±0.03	0.24±0.04	0.26±0.04	0.40±0.05	0.40±0.05
3.0	3.5	0.07±0.02	0.05±0.02	0.09±0.02	0.08±0.02	0.17±0.03	0.18±0.04
3.5	4.0	0.02±0.01	0.01±0.01	0.02±0.01	0.03±0.01	0.07±0.02	0.05±0.02
4.0	4.5	–	–	–	–	0.01±0.01	0.01±0.01

Table 20: Normalized cms-rapidity distribution $\rho(y^*)$ for positive and negative hadrons in μXe scattering.

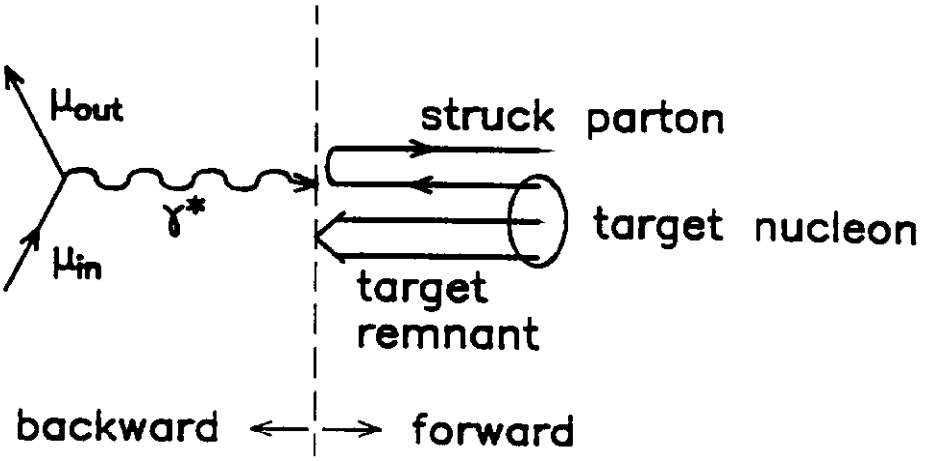

Fig. 1: Deep-inelastic muon-nucleon scattering in the quark-parton model, as viewed in the hadronic center-of-mass system.

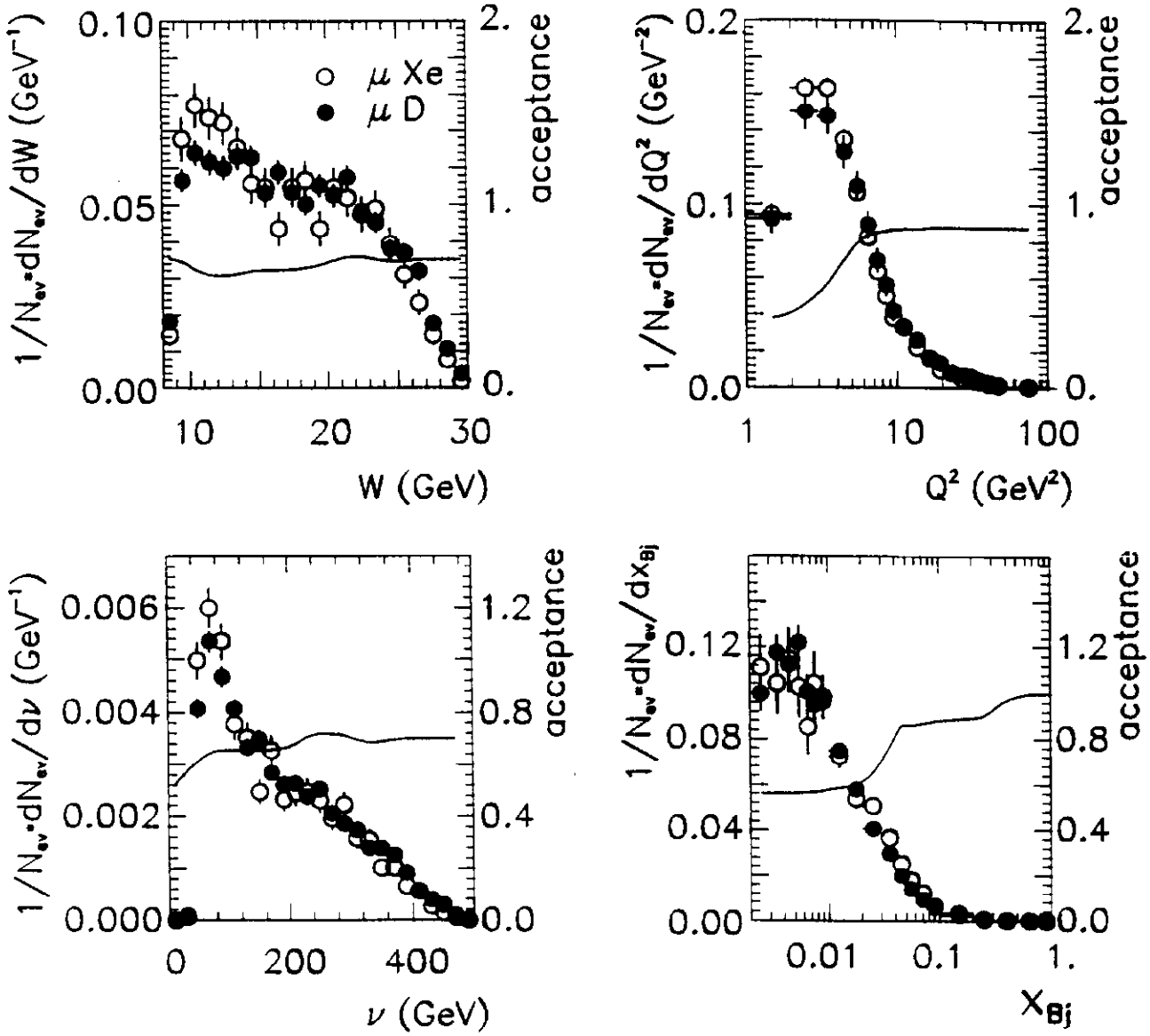

Fig. 2: Raw distributions of W, Q^2, ν and x_{Bj} for the samples of all μD (full circles) and all μXe (open circles) events in the kinematic region defined by eq. (2). The acceptance (= number of reconstructed MC events divided by the number of generated MC events) is drawn as a solid line. The scales on the left hand side of the figures refer to the raw distributions, those on the right hand side to the acceptance.

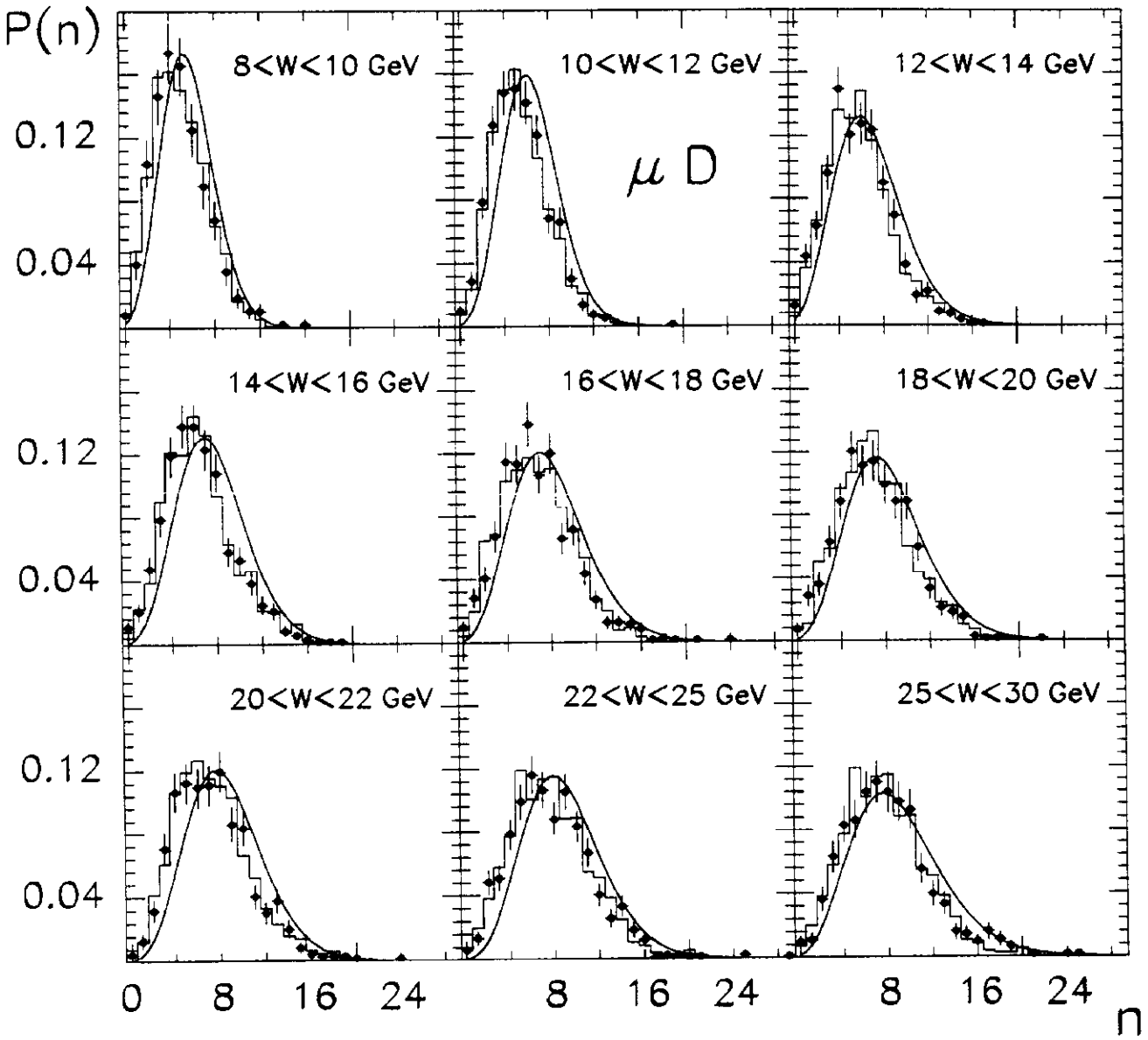

Fig. 3: Raw multiplicity distributions in different bins of W for μD scattering. The lines represent the fitted theoretical distributions, assuming a negative binomial parametrization: solid line = unsmeared theoretical distribution, histogram = smeared theoretical distribution.

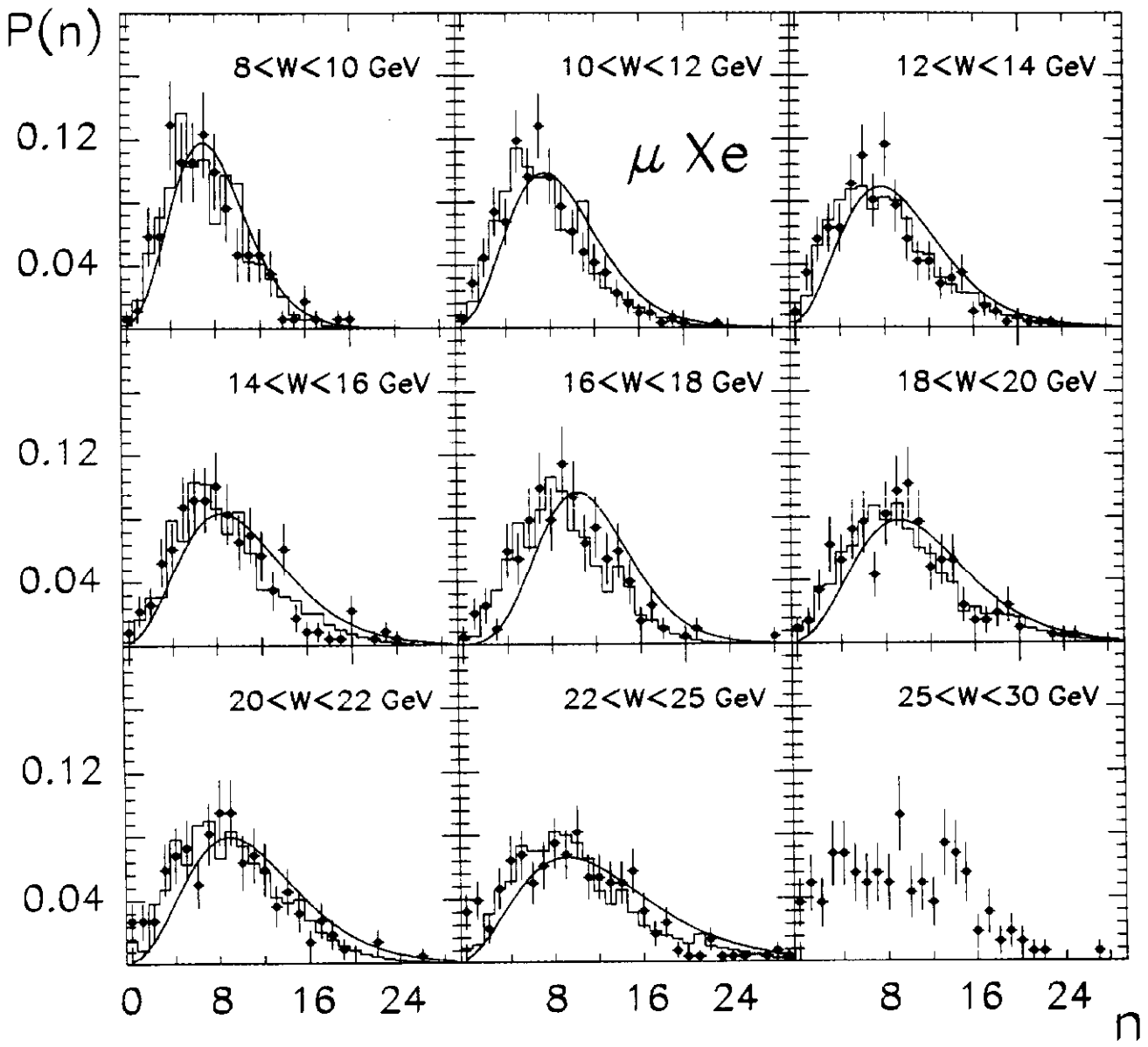

Fig. 4: Raw multiplicity distributions in different bins of W for μXe scattering. The lines represent the fitted theoretical distributions, assuming a negative binomial parametrization: solid line = unsmeared theoretical distribution, histogram = smeared theoretical distribution.

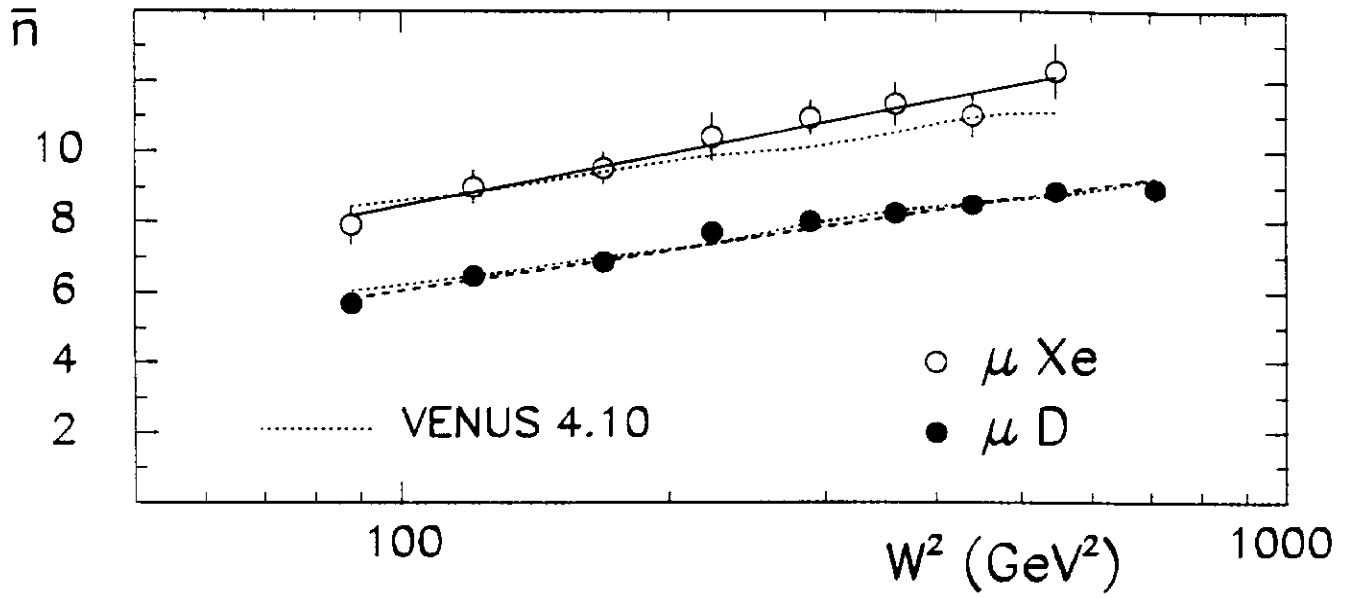

Fig. 5: Average multiplicity $\bar{n}$ as a function of W^2 for μD (full circles) and μXe scattering (open circles). The results from straight line fits to the data points are drawn as dashed and solid lines. The dotted lines represent the predictions of the VENUS model.

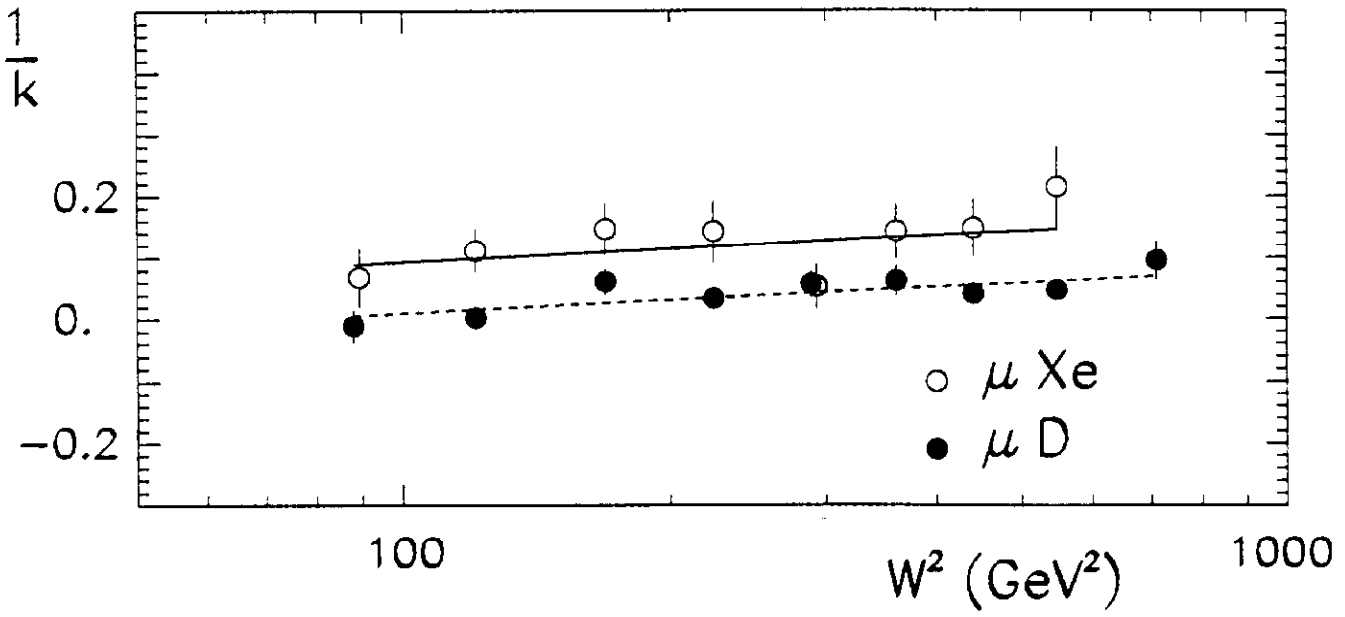

Fig. 6: 1/k as a function of W^2 for μD (full circles) and μXe scattering (open circles). The results from straight line fits to the data points are drawn as dashed and solid lines.

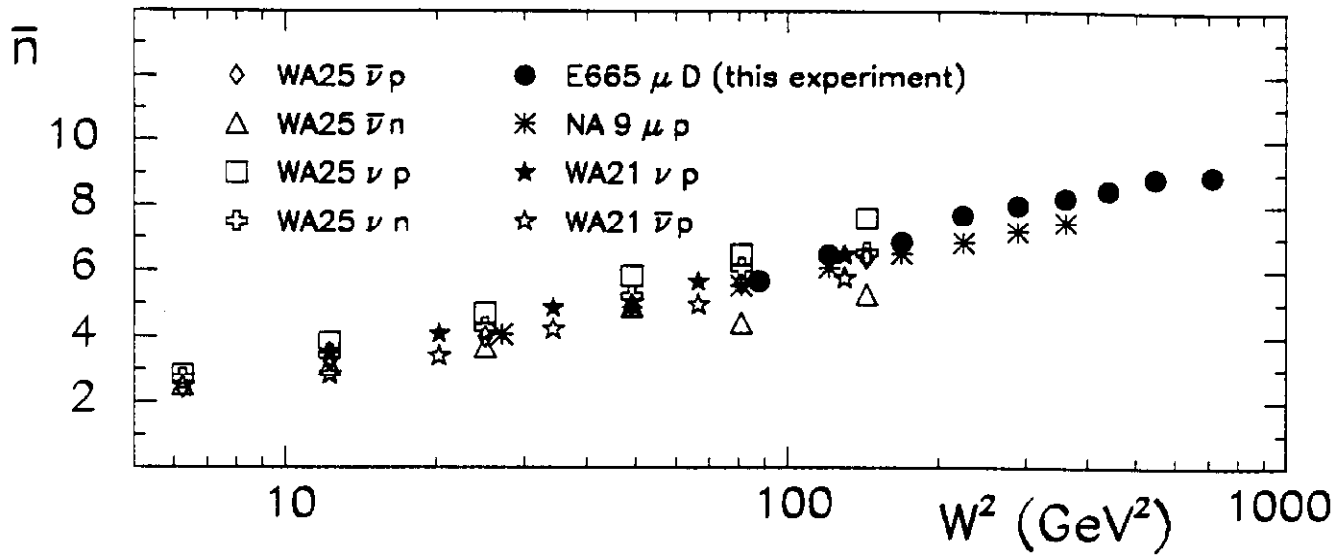

Fig. 7: Average multiplicity $\bar{n}$ as a function of W^2 for various lepton-nucleon experiments: νp and $\bar{\nu}p$ from WA21 [39], νp, νn, $\bar{\nu}p$, $\bar{\nu}n$ from WA25 [40], μp from NA9 [1] and μD from this experiment (E665).

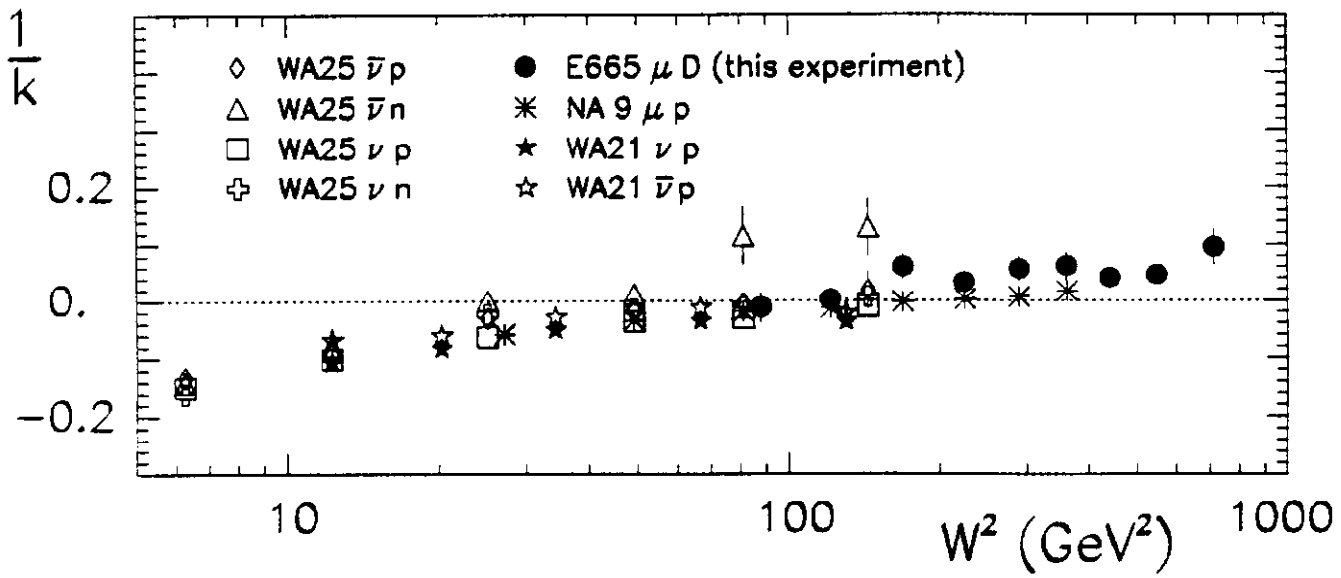

Fig. 8: $1/k$ as a function of W^2 for various lepton-nucleon experiments: νp and $\bar{\nu}p$ from WA21 [39], νp, νn, $\bar{\nu}p$, $\bar{\nu}n$ from WA25 [40], μp from NA9 [1] and μD from this experiment (E665).

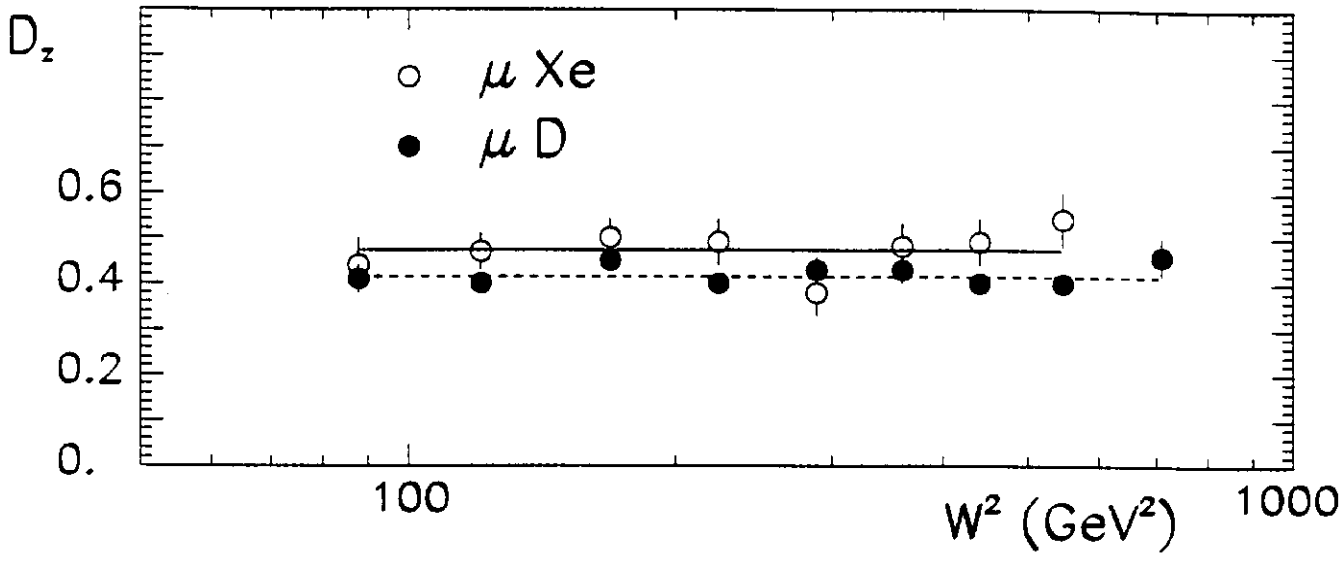

Fig. 9: Dispersion D_z^{NBD} of the scaled multiplicity $z = n/\bar{n}$, obtained from fits of the negative binomial function, as a function of W^2 for μD (full circles) and μXe scattering (open circles). The data points were fitted by a constant, represented by the dashed and solid lines.

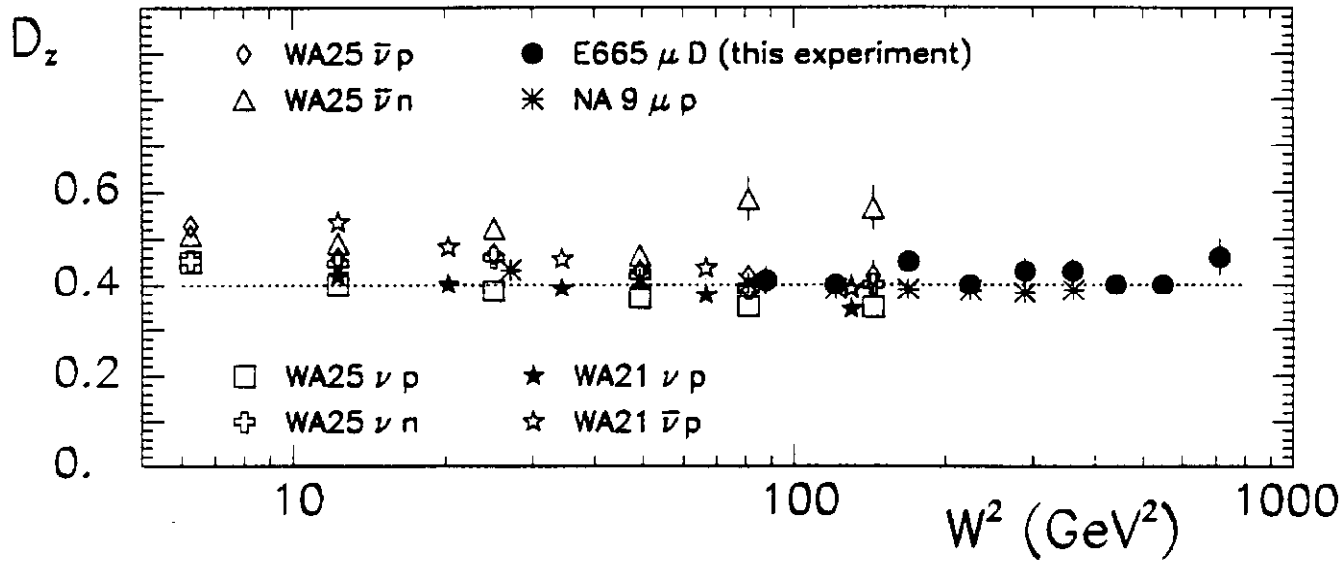

Fig. 10: Dispersion D_z^{NBD} of the scaled multiplicity $z = n/\bar{n}$, obtained from fits of the negative binomial function, as a function of W^2 for various lepton-nucleon experiments: νp and $\bar{\nu}p$ from WA21 [39], νp, νn, $\bar{\nu}p$, $\bar{\nu}n$ from WA25 [40], μp from NA9 [1] and μD from this experiment (E665). The straight line at $D_z = 0.4$ is drawn to guide the eye.

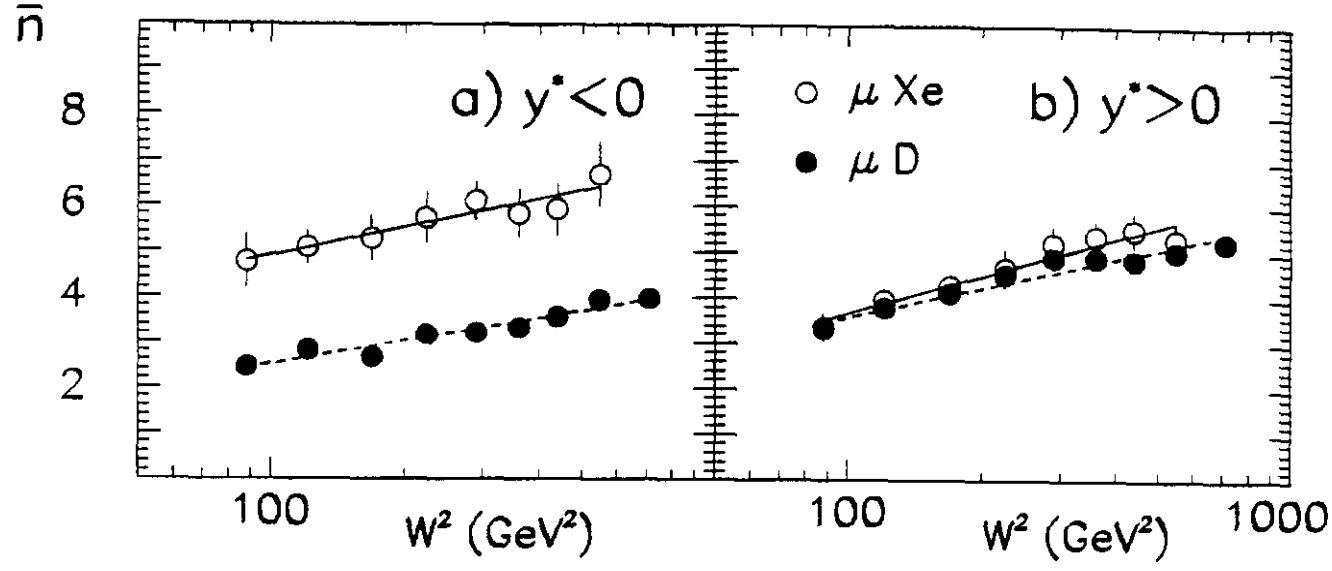

Fig. 11: Average multiplicity $\bar{n}$ for the backward (a) and forward (b) hemispheres as a function of W^2 for μD (full circles) and μXe scattering (open circles). The results of straight-line fits to the data points are drawn as dashed and solid lines.

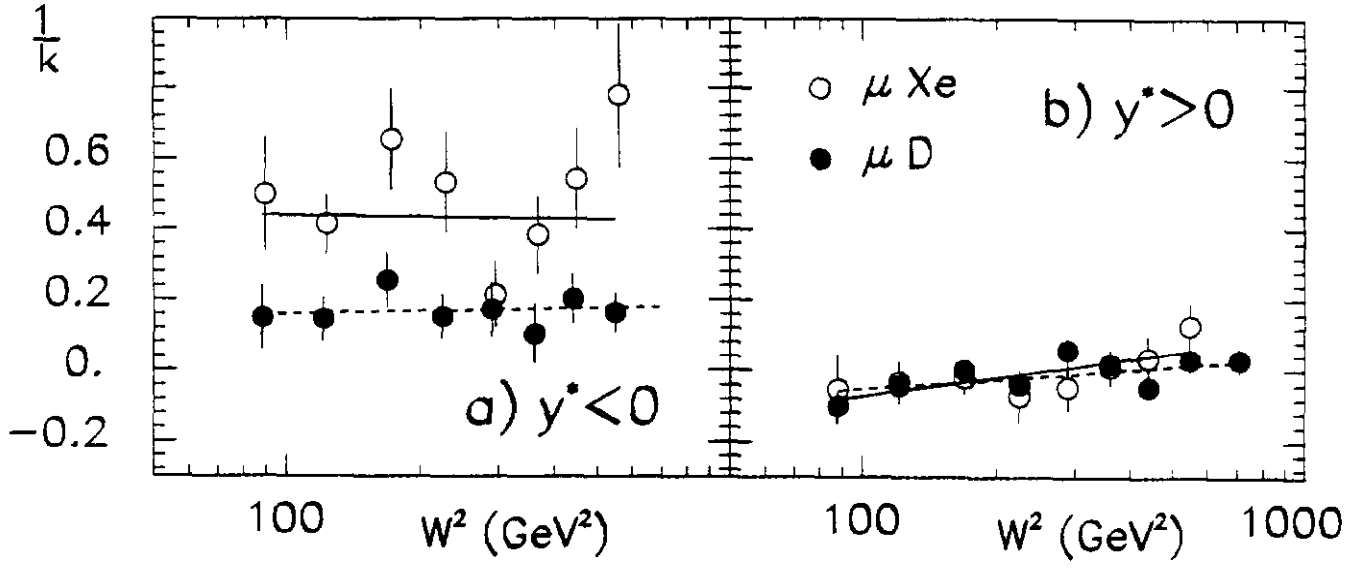

Fig. 12: $1/k$ for the backward (a) and forward (b) hemispheres as a function of W^2 for μD (full circles) and μXe scattering (open circles). The results of straight-line fits to the data points are drawn as dashed and solid lines.

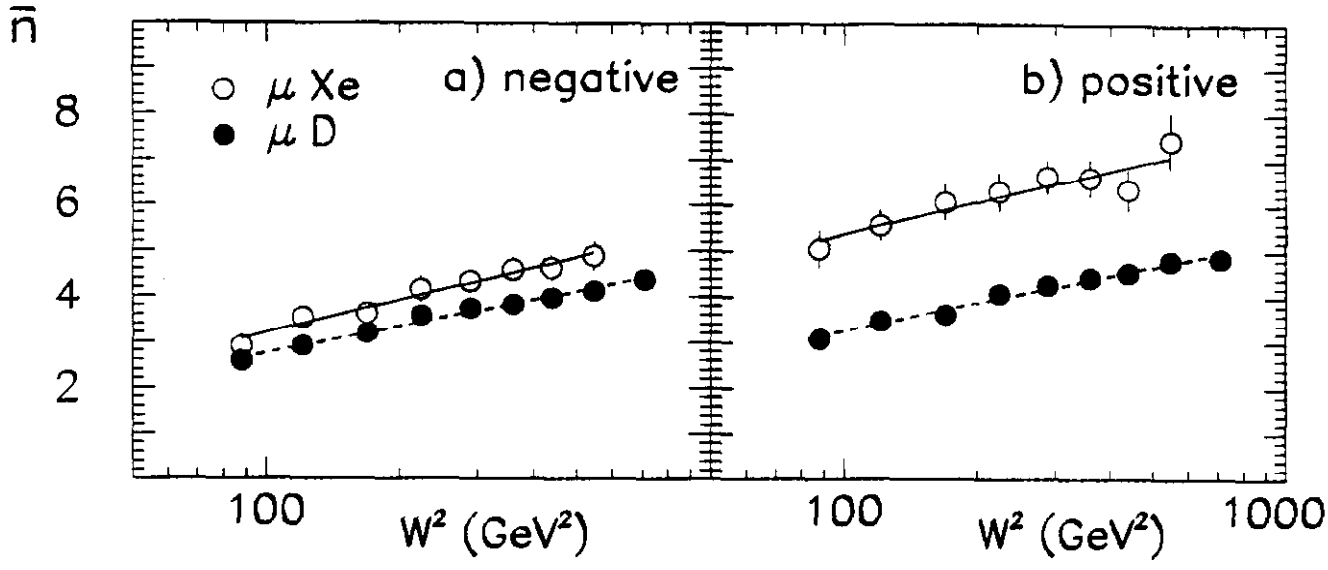

Fig. 13: Average multiplicity $\bar{n}$ for negative (a) and positive (b) hadrons as a function of W^2 for μD (full circles) and μXe scattering (open circles). The results of straight-line fits to the data points are drawn as dashed and solid lines.

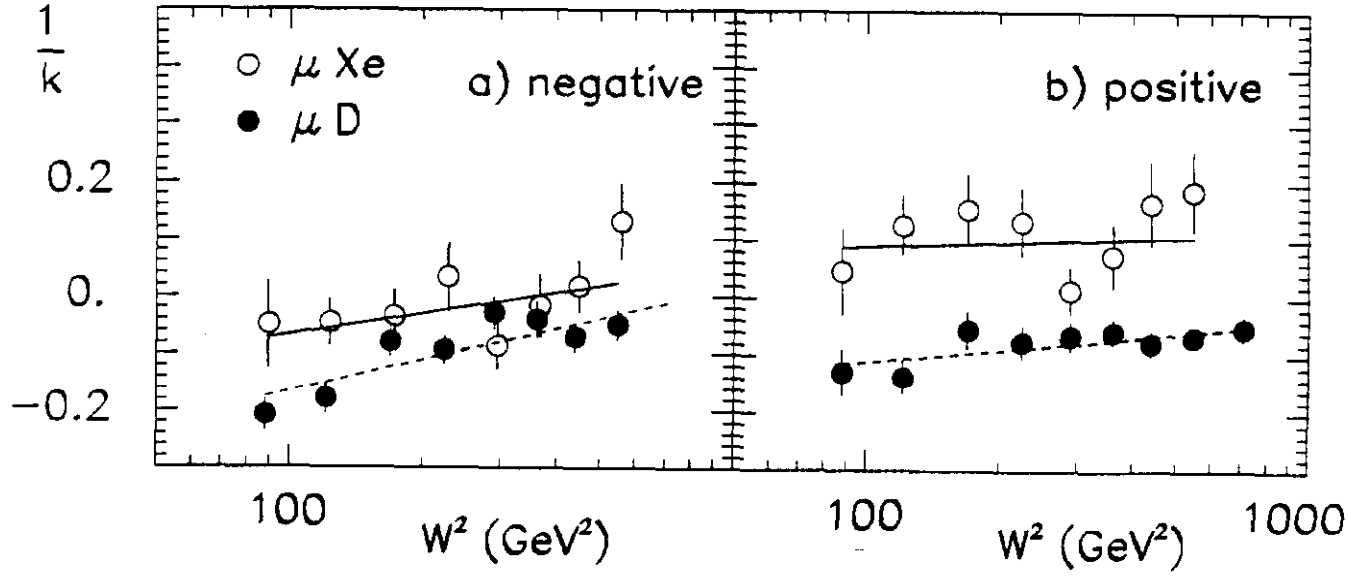

Fig. 14: $1/k$ for negative (a) and positive (b) hadrons as a function of W^2 for μD (full circles) and μXe scattering (open circles). The results of straight-line fits to the data points are drawn as dashed and solid lines.

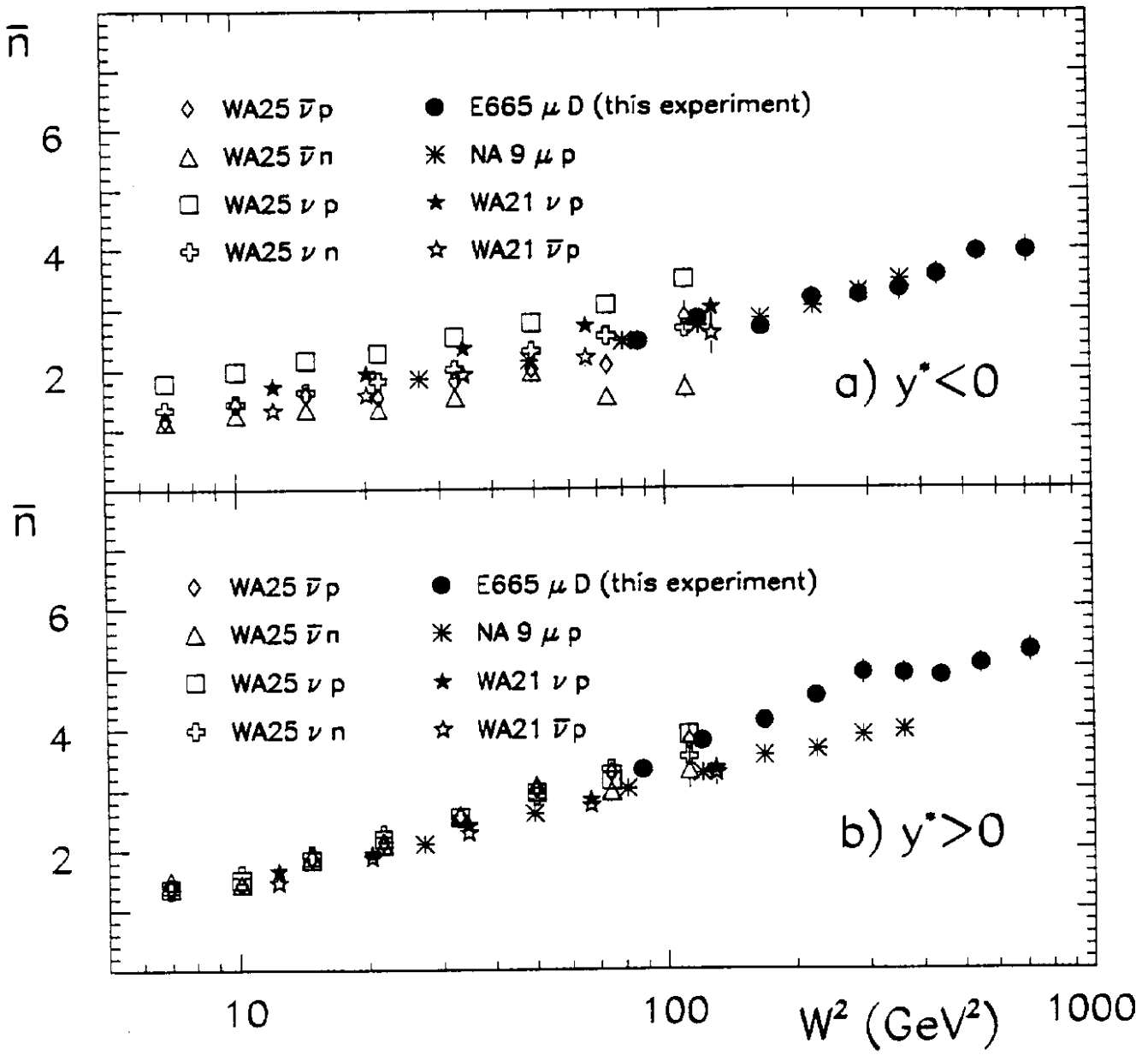

Fig. 15: Average backward (a) and forward (b) multiplicity as a function of W^2 for various lepton-nucleon experiments: νp and $\bar{\nu}p$ from WA21 [39], $\nu p, \nu n, \bar{\nu}p, \bar{\nu}n$ from WA25 [47], μp from NA9 [1] and μD from this experiment (E665).

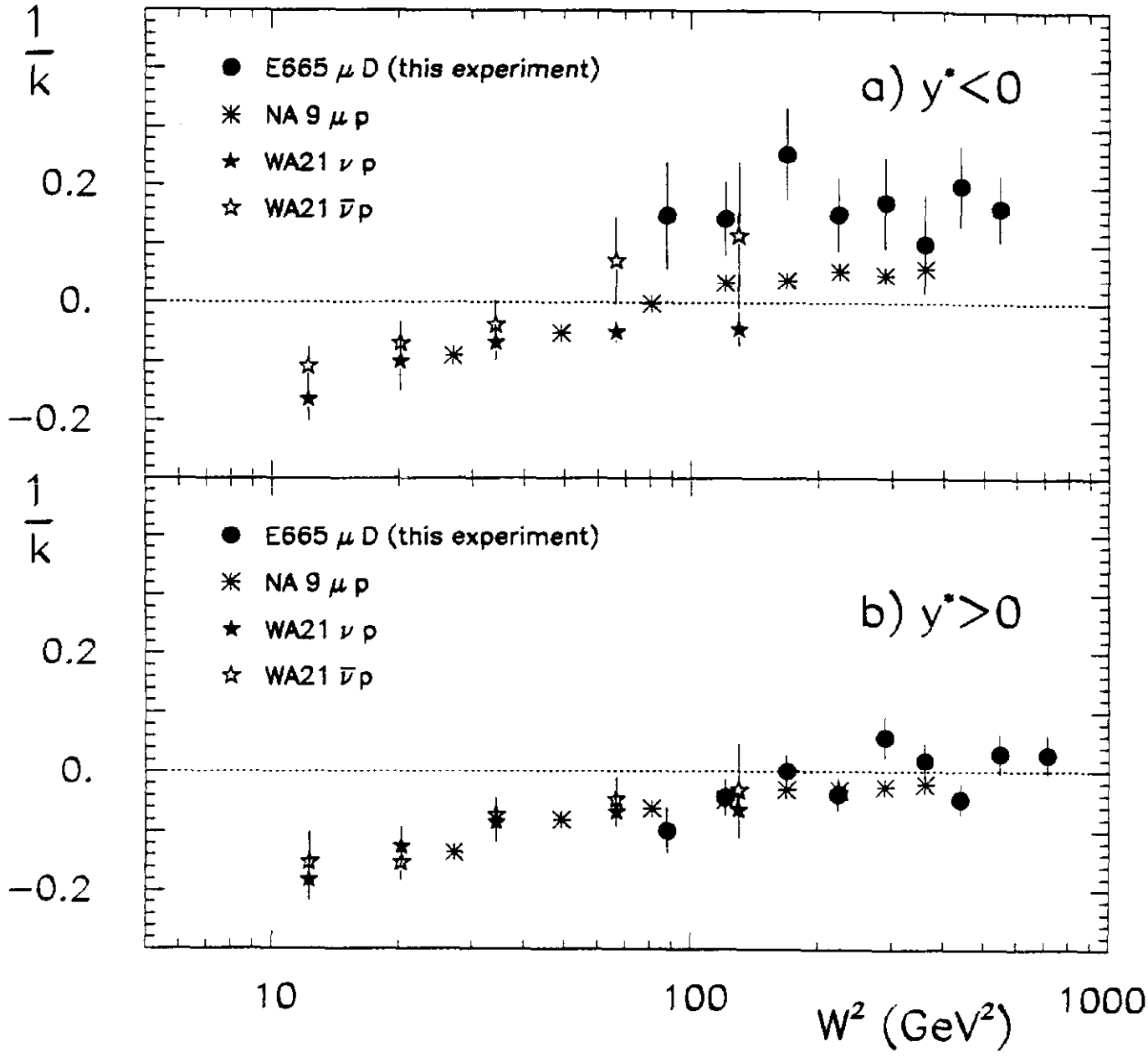

Fig. 16: $1/k$ for the backward (a) and forward (b) hemispheres as a function of W^2 for (anti-)neutrino proton [39], μp [1] and μD scattering (E665).

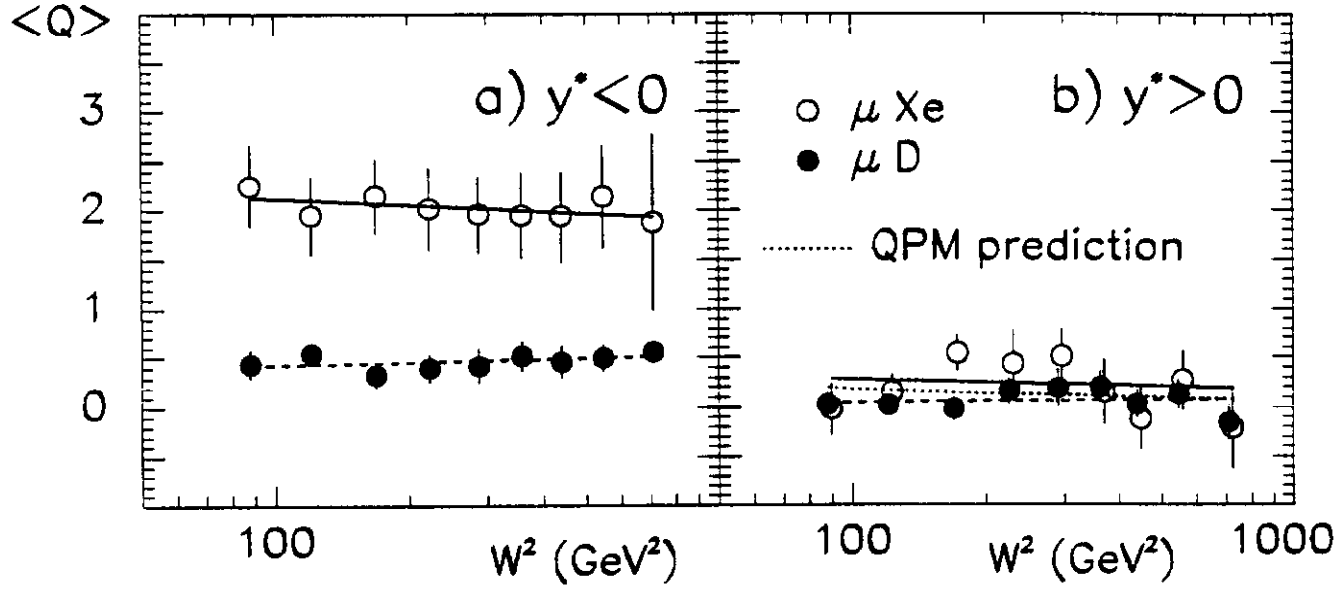

Fig. 17: Average hadronic net charge $\langle Q \rangle$ as a function of W^2 for the backward (a) and forward (b) hemispheres, for μD (full circles) and μXe scattering (open circles). The dashed and solid lines are the results of straight-line fits to the data points. The dotted line in (b) represents the prediction of the QPM for the average hadronic forward charge (eq. (12)).

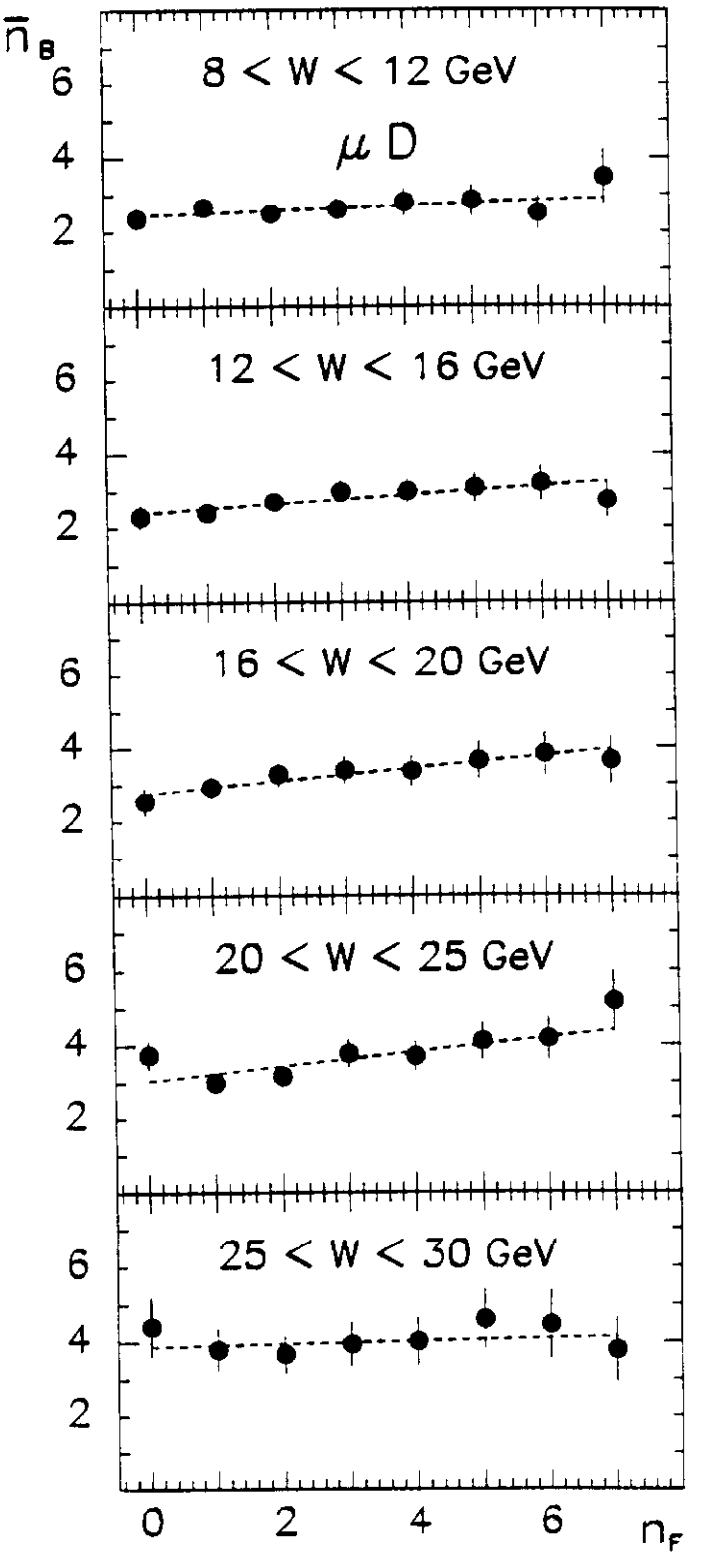

Fig. 18: Average backward multiplicity as a function of the forward multiplicity in different bins of W, for μD scattering. The dashed lines are the results of straight-line fits to the data points.

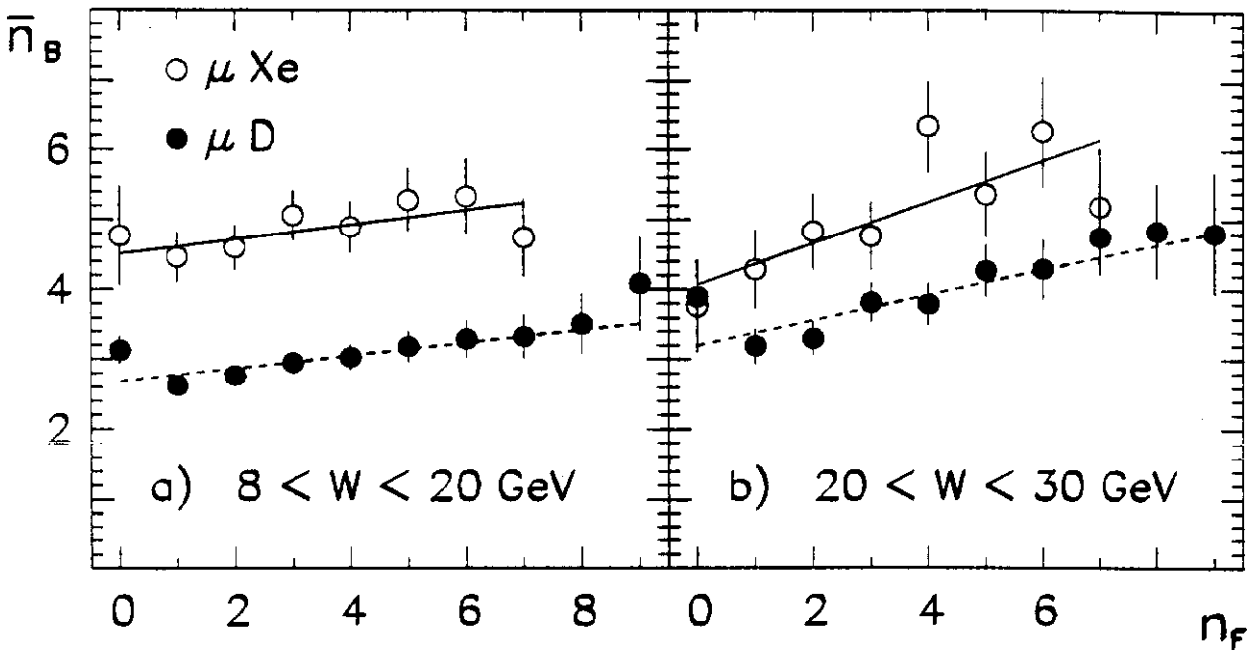

Fig. 19: Average backward multiplicity as a function of the forward multiplicity for μD (full circles) and μXe (open circles) scattering, in two bins of W. The dashed and solid lines are the results of straight-line fits to the data points.

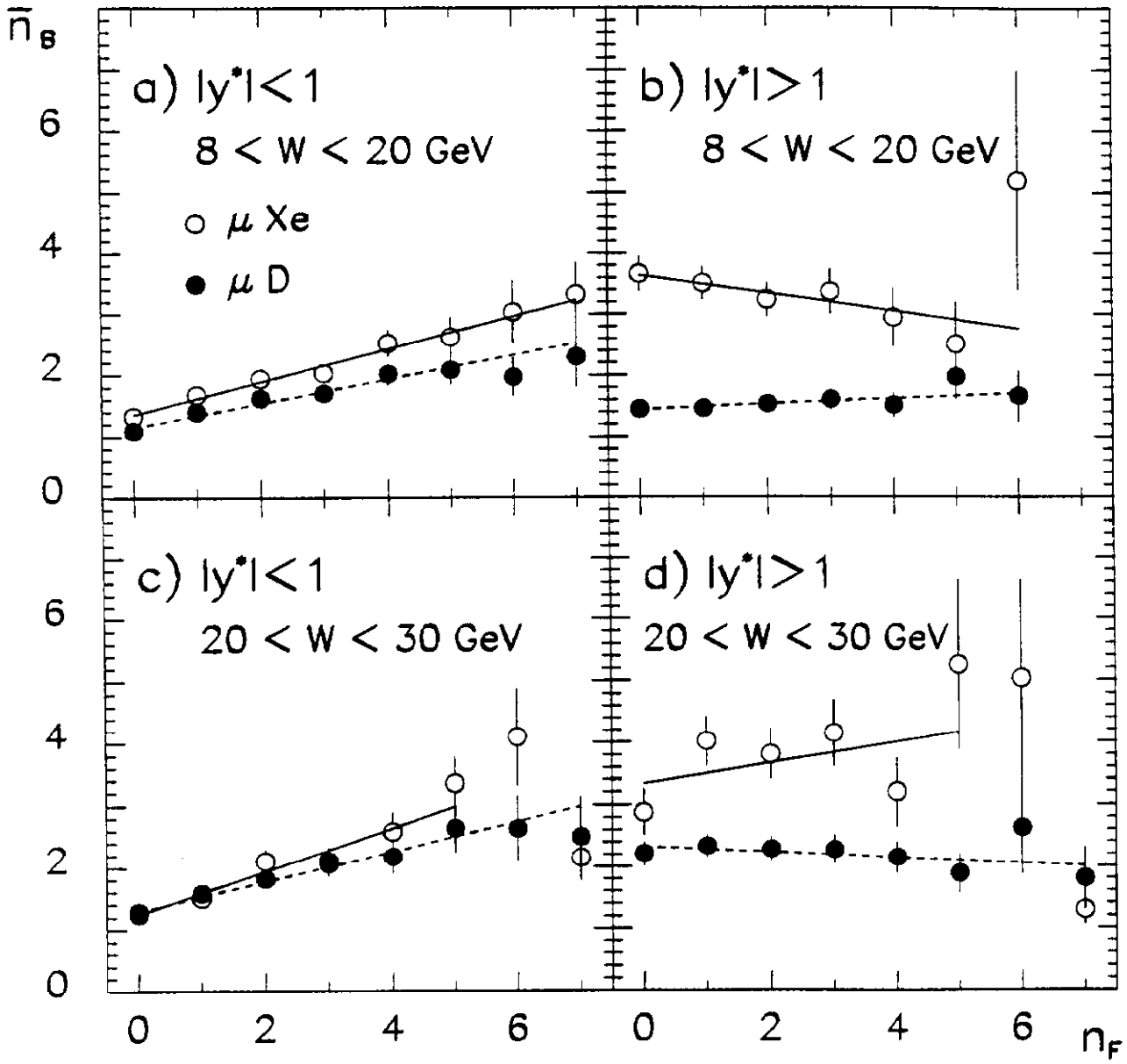

Fig. 20: Average backward multiplicity as a function of the forward multiplicity for a central and an outer cms-rapidity range, for μD (full circles) and μXe (open circles) scattering, in two bins of W. The dashed and solid lines are the results of straight-line fits to the data points.

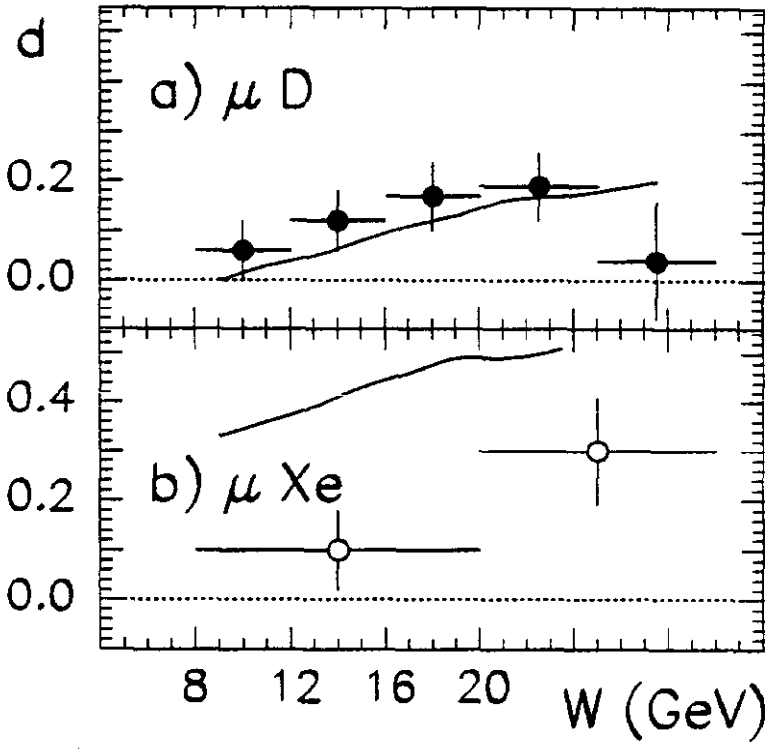

Fig. 21: Forward-backward correlation parameter d as a function of W, for μD (a) and μXe (b) scattering. The solid curves correspond to the expectation (17) for random forward-backward partitioning of particles.

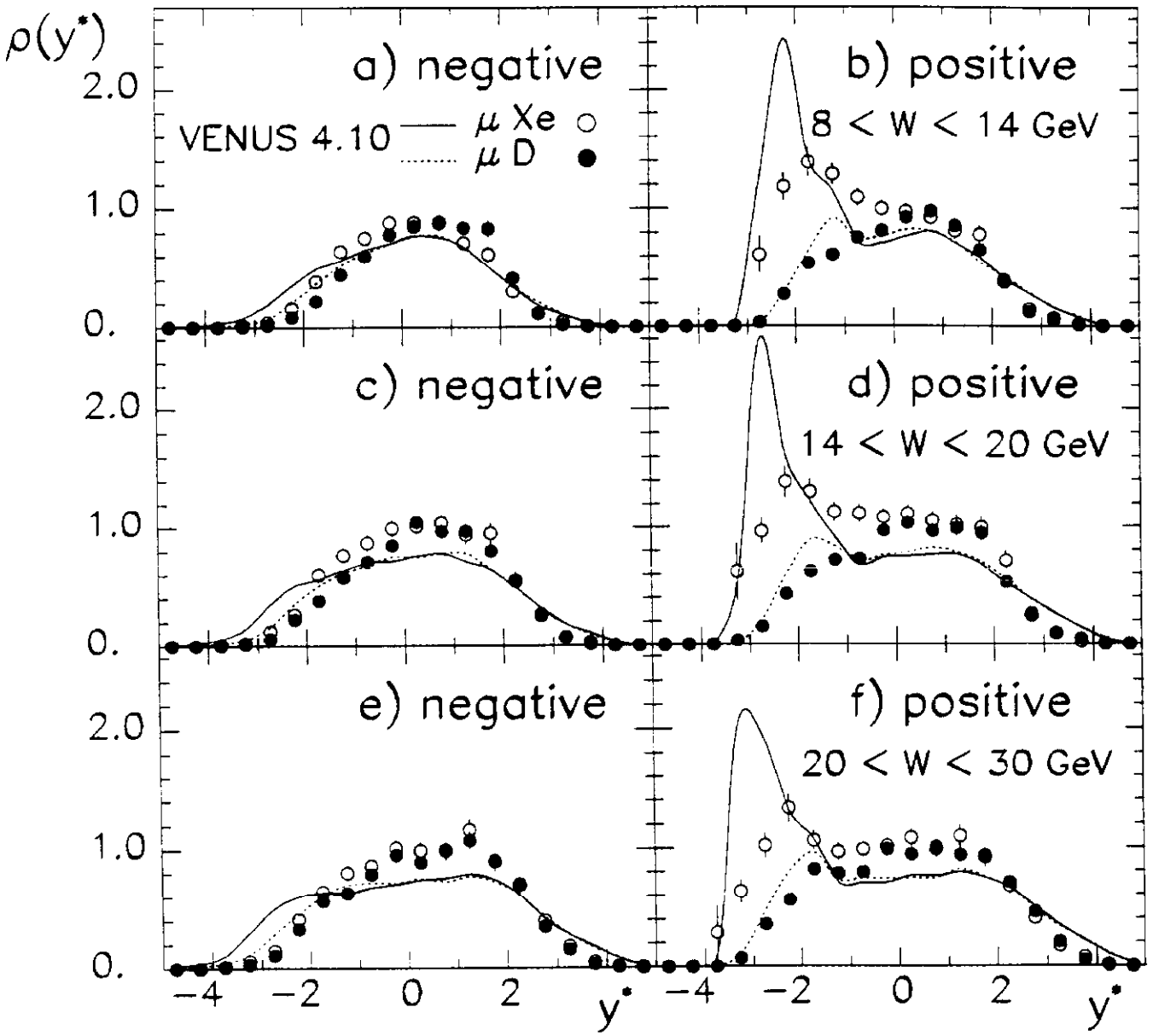

Fig. 22: Normalized cms-rapidity distribution of negative and positive hadrons, for μD (full circles) and μXe scattering (open circles), in three bins of W. The lines represent the predictions of the VENUS model for μD (dotted lines) and μXe scattering (solid lines). It should be noted that the distribution for positive hadrons in μXe scattering has a systematic error, the size of which can be estimated from the distributions in Fig. 23.

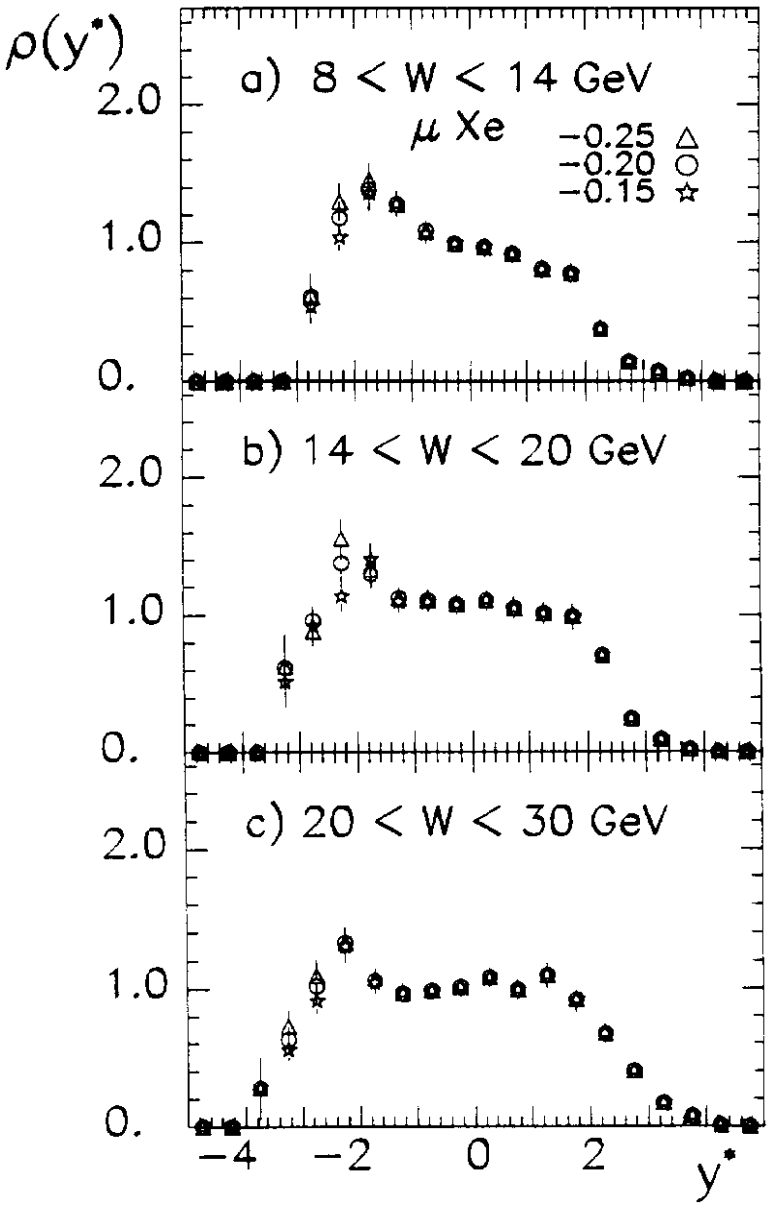

Fig. 23: Normalized cms-rapidity distribution of positive hadrons in μXe scattering, in three bins of W, for three variants of the particle identification procedure (see Sect. 3.1): assignment of the proton mass if $x_F(m_\pi)$ is < -0.15 (stars), or if $x_F(m_\pi)$ is < -0.20 (circles), or if $x_F(m_\pi)$ is < -0.25 (triangles).

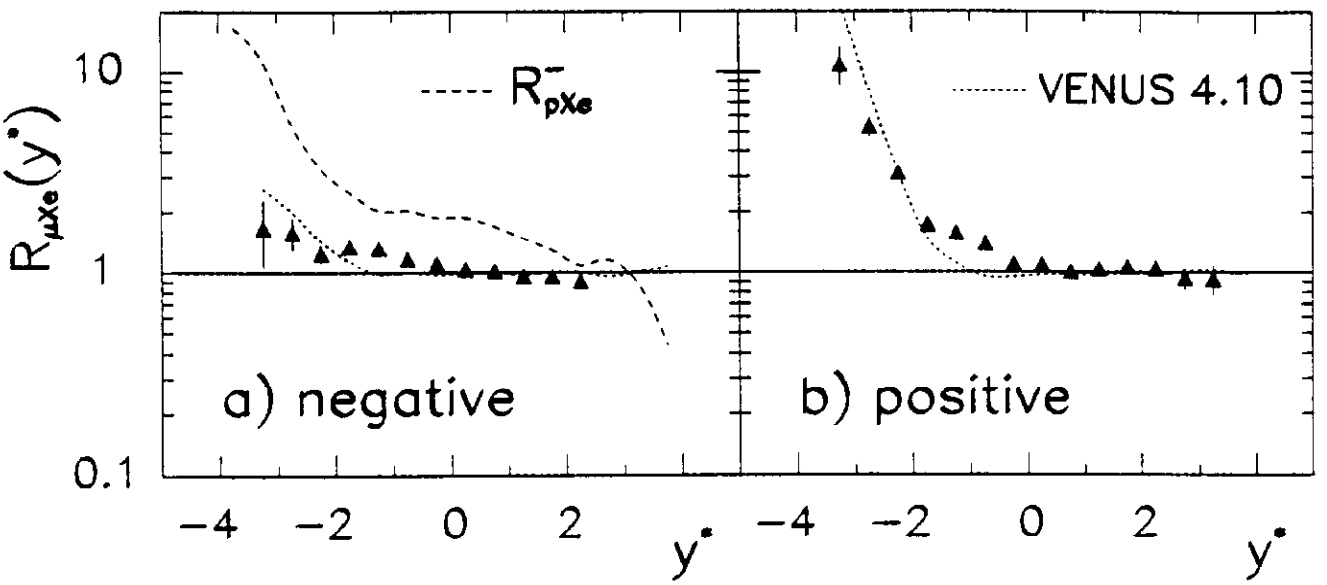

Fig. 24: Ratio $R_{\mu\mathrm{Xe}}(y^*) = \rho(y^*)_{\mu\mathrm{Xe}}/\rho(y^*)_{\mu\mathrm{D}}$ of the normalized cms-rapidity distributions in μXe and μD scattering, for negative (a) and positive (b) hadrons. The dotted lines represent the predictions of the VENUS model. The dashed line in (a) is the ratio $R^-_{p\mathrm{Xe}}$ from ref. [53]. In [53] $R^-_{p\mathrm{Xe}}$ is given as a function of the lab-rapidity y_{lab}, which in good approximation is related to y^* by $y^* \approx y_{lab} - 3.0$.

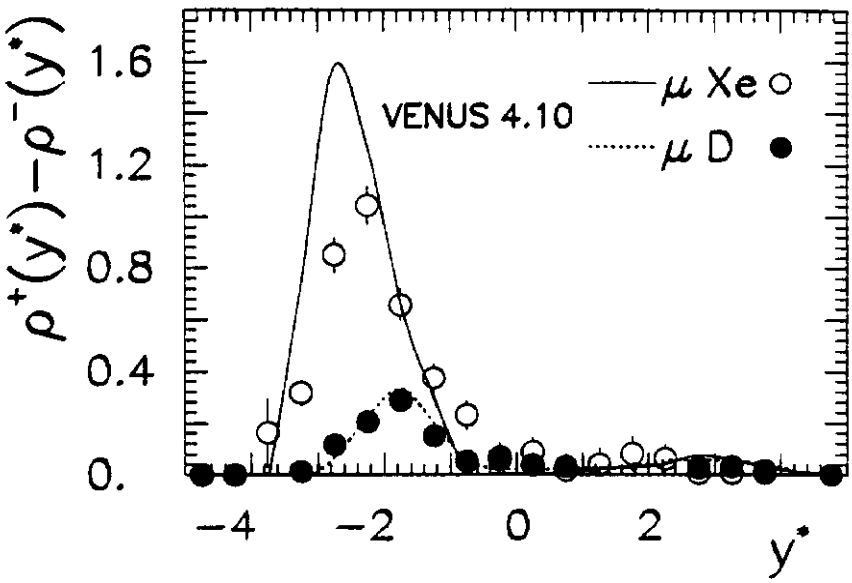

Fig. 25: Normalized cms–rapidity distribution of the hadronic net charge for μD (full circles) and μXe scattering (open circles). The lines represent the predictions of the VENUS model.

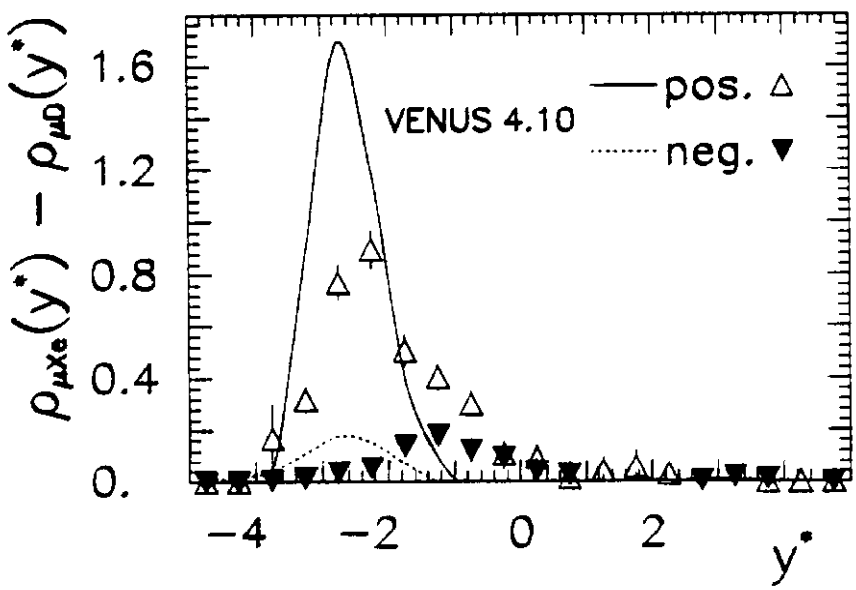

Fig. 26: Difference of the normalized cms-rapidity distributions between μXe and μD scattering, for positive (open triangles) and negative hadrons (full triangles). The lines represent the predictions of the VENUS model.

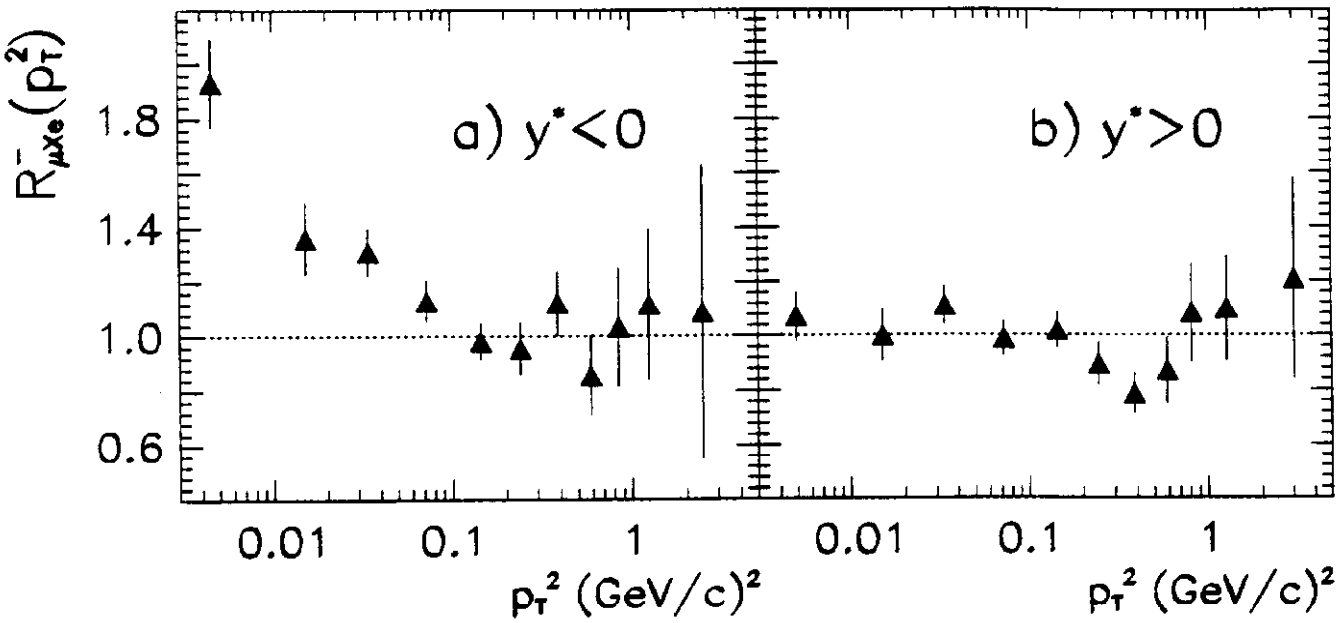

Fig. 27: Ratio $R^-_{\mu Xe}(p_T^2) = \rho^-(p_T^2)_{\mu Xe}/\rho^-(p_T^2)_{\mu D}$ of the normalized p_T^2 distributions of negative hadrons for μXe and μD scattering. a) backward hemisphere, b) forward hemisphere. It should be noted that the data points for $p_T^2 \leq 0.02$ (GeV/c)^2 have large systematic errors ($\approx 20\%$) (see Sect. 3.2).

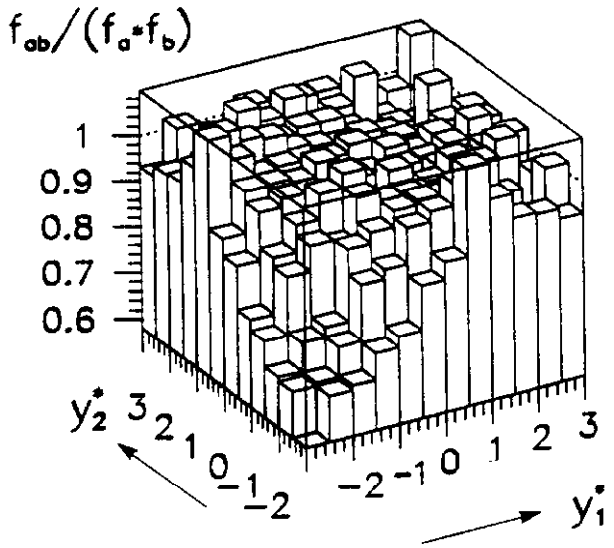

Fig. 28: Correction factor $f_{ab}/(f_a \cdot f_b)$ for the correlation term $\rho^{ab}(y_1^*, y_2^*)/(\rho^a(y_1^*) \cdot \rho^b(y_2^*))$ for charged hadrons, plotted as a function of y_1^* and y_2^*.

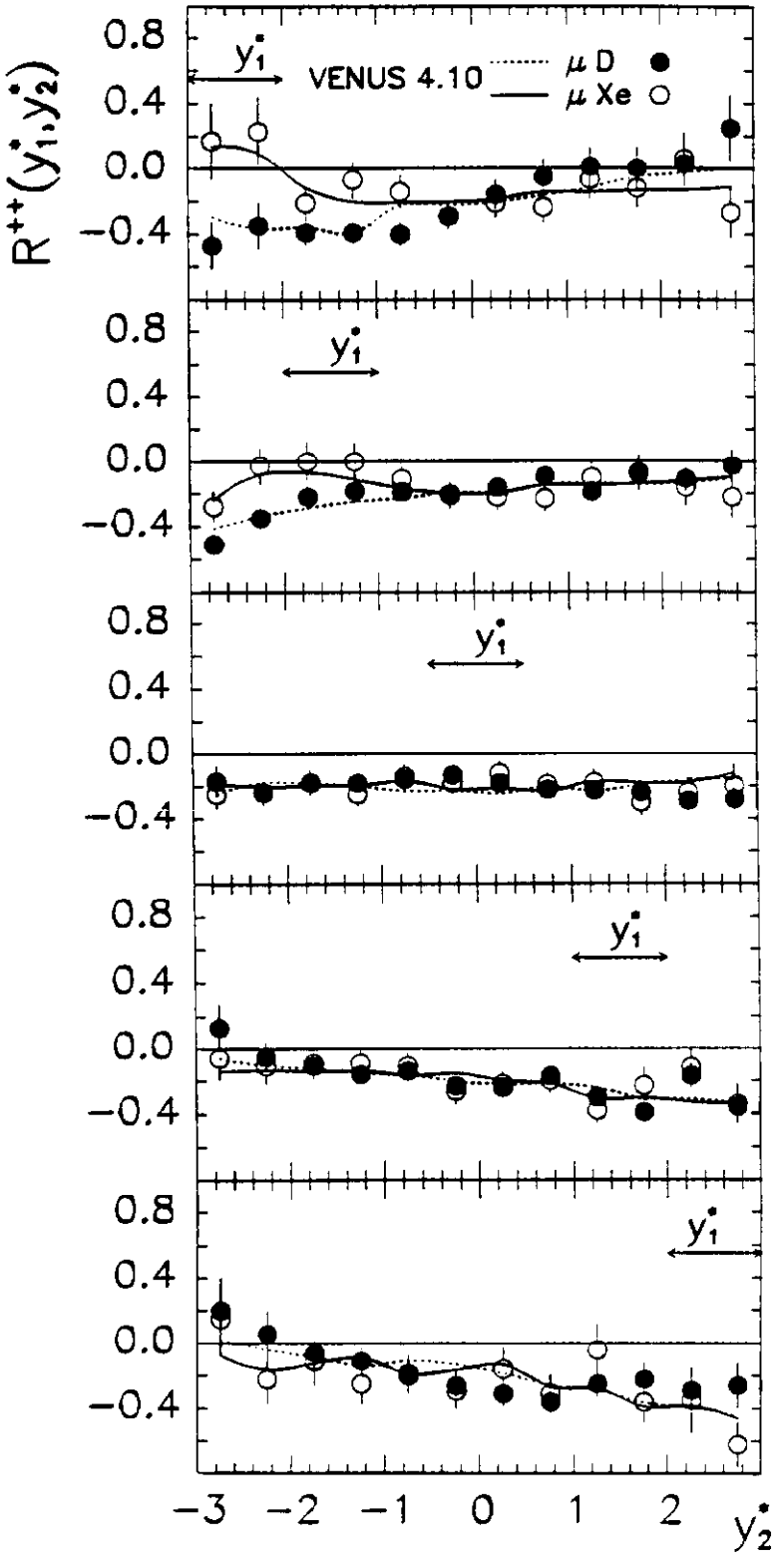

Fig. 29: Correlation function $R^{++}(y_1^*, y_2^*)$ as a function of y_2^* for μD (full circles) and μXe scattering (open circles), for different bins of y_1^*. The position of the y_1^* bin is indicated by an arrow ($\longleftrightarrow$). The lines represent the predictions of the VENUS model for μD (dotted line) and for μXe scattering (solid line). The charged multiplicity was restricted to the region 6 to 10.

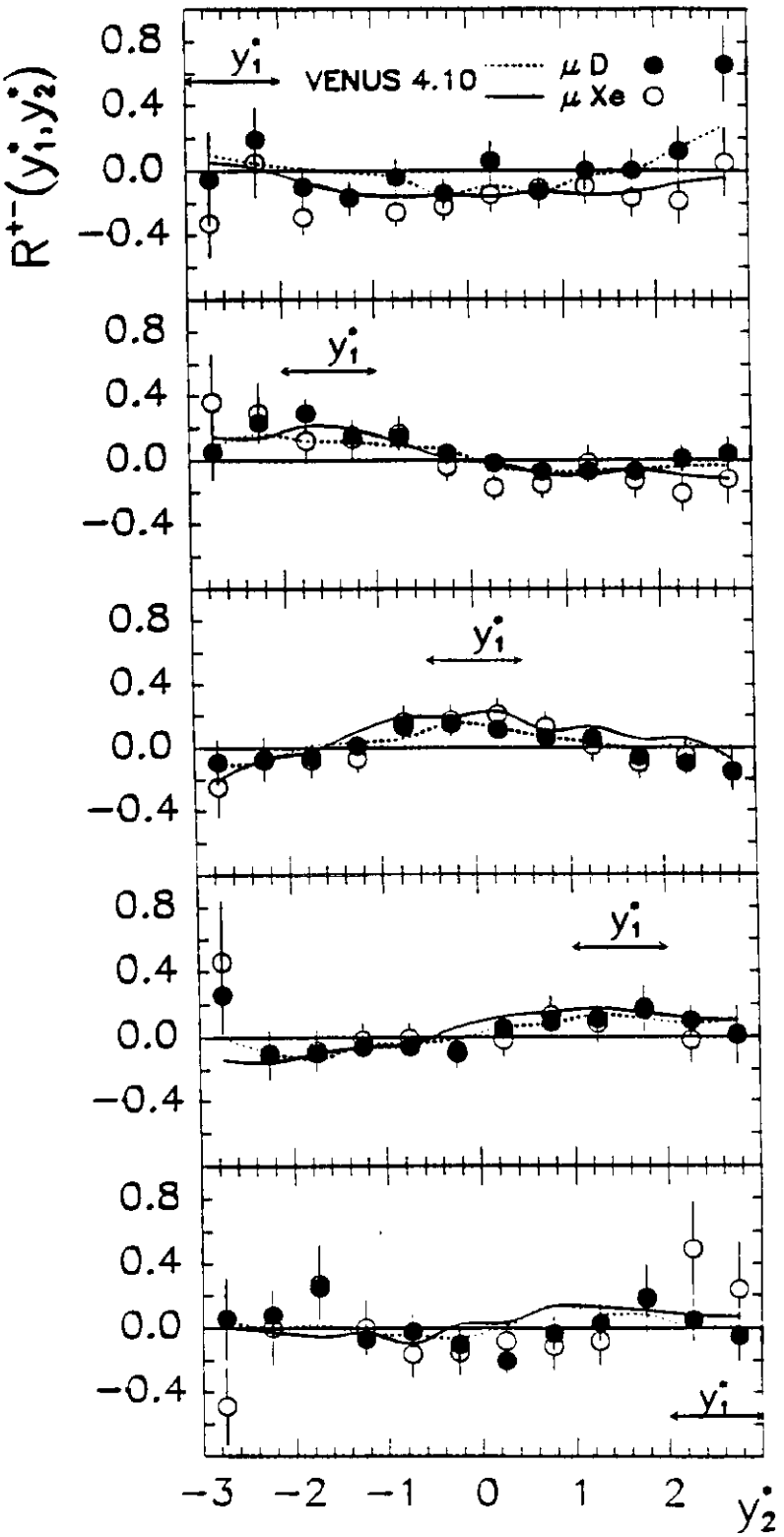

Fig. 30: Correlation function $R^{+-}(y_1^*, y_2^*)$ as a function of y_2^* for μD (full circles) and μXe scattering (open circles), for different bins of y_1^* of the positive hadron. The position of the y_1^* bin is indicated by an arrow ($\longleftrightarrow$). The lines represent the predictions of the VENUS model for μD (dotted line) and for μXe scattering (solid line). The charged multiplicity was restricted to the region 6 to 10.